A guanidine-based coronavirus replication inhibitor which targets the nsp15 endoribonuclease and combines a direct antiviral effect with subtle boosting of interferon

Benjamin Van Loy[1], Eugènia Pujol[2,3], Kenichi Kamata[4#], Xiao Yin Lee[4], Nikolai Bakirtzoglou[1], Ria Van Berwaer[1], Julie Vandeput[1], Leentje Persoons[1], Brent De Wijngaert[1], Quinten Goovaerts[1], Sam Noppen[1], Kourosh Ahmadzadeh[1], Juan Martín-López[2,3], Celia Escriche[2,3], Bert Vanmechelen[1], Besir Krasniqi[5†], Abhimanyu K. Singh[1‡], Piet Maes[1], Patrick Matthys[1], Wim Dehaen[5], Jef Rozenski[6], Kalyan Das[1], Arnout Voet[4], Santiago Vázquez[2,3], Lieve Naesens[1*] and Annelies Stevaert[1]

[1]Rega Institute, Department of Microbiology, Immunology and Transplantation, KU Leuven, Leuven, Belgium

[2]Laboratori de Química Farmacèutica (Unitat Associada al Consejo Superior de Investigaciones Científicas), Facultat de Farmàcia i Ciències de l'Alimentació, Universitat de Barcelona, Barcelona, Spain

[3]Institute of Biomedicine of the University of Barcelona (IBUB), Universitat de Barcelona, Barcelona, Spain

[4]Biochemistry, Molecular and Structural Biology, Department of Chemistry, KU Leuven, Leuven, Belgium

[5]Sustainable Chemistry for Metals and Molecules, Department of Chemistry, KU Leuven, Leuven, Belgium

[6]Rega Institute, Department of Pharmaceutical and Pharmacological Sciences, KU Leuven, Leuven, Belgium

[#]Current address: Yokohama City University, Yokohama, Japan

[†]Current address: Vlaamse Instelling voor Technologisch Onderzoek (VITO), Mol, Belgium

[‡]Current address: Mahatma Gandhi Medical Advanced Research Institute, Sri Balaji Vidyapeeth, Puducherry, India

*Corresponding author

E-mail: lieve.naesens@kuleuven.be (LN)

Short title

Coronavirus replication inhibitor targeting the nsp15 endoribonuclease

Abstract

The approval of COVID-19 vaccines and two classes of antiviral drugs has been crucial in addressing the global health crisis caused by SARS-CoV-2. However, to prepare for future outbreaks from drug-resistant variants and novel zoonotic coronaviruses (CoVs), additional therapeutics with a distinct antiviral mechanism are needed. Here, we report a novel guanidine-substituted diphenylurea compound that suppresses CoV replication by interfering with the uridine-specific endoribonuclease (EndoU) activity of the viral non-structural protein-15 (nsp15). This compound, designated EPB-113, exhibits strong and selective cell culture activity against human coronavirus 229E (HCoV-229E) and also suppresses the replication of SARS-CoV-2. HCoV-229E viruses selected for resistance to EPB-113 carried mutations at or near the catalytic residue His250 in the nsp15 EndoU domain. EndoU is known to reduce the levels of viral dsRNA and avoid induction of type I interferon (IFN-I). Accordingly, the mutant viruses selected under EPB-113 were unable to replicate in human macrophages and were readily outcompeted by the wild-type virus upon co-infection of human fibroblast cells. This highlights the critical role of EndoU in maintaining CoV replication. By targeting nsp15, EPB-113 combines a direct antiviral effect with subtle boosting of IFN-I. Using a combination of biophysical and enzymatic assays with the recombinant nsp15 proteins from HCoV-229E and SARS-CoV-2, we discovered that EPB-113 reduces the thermal stability of hexameric nsp15, while enhancing its EndoU cleavage activity. This EndoU-stimulating mechanism offers an explanation why the virus escapes EPB-113 by becoming EndoU-deficient. Our findings suggest that targeting nsp15 as an antiviral strategy may require a mechanism that alters the conformation of this protein and disrupts its EndoU activity and other functions related to immune evasion and viral replication. Based on the appealing pharmacological profile of EPB-113, we conclude that nsp15 is a challenging but highly relevant drug target.

Author summary

Despite significant progress in controlling the global COVID-19 crisis through vaccines and antiviral drugs, SARS-CoV-2 infection remains a serious health threat for vulnerable individuals, such as elderly and immunocompromised patients. These populations could benefit from innovative treatments that target the virus from multiple angles. In this study, we focus on the nsp15 endoribonuclease (EndoU), a poorly understood coronavirus protein that aids in viral evasion from the host innate immune response and is assumed to regulate viral RNA synthesis. Our research centers around a newly identified, first-in-class coronavirus inhibitor, designated EPB-113, which specifically targets nsp15. This compound has the unique property to suppress the virus in two complementary ways via subtle induction of interferon combined with a direct impact on viral RNA synthesis. EPB-113 selects for escape mutants that carry substitutions in the core of EndoU, leading to a severe replication defect. When incubated with nsp15 protein, EPB-113 induces a structural change and enhances its EndoU enzyme activity. Hence, our study introduces a novel drug concept that disrupts the multifunctional nsp15 protein and suppresses coronavirus replication on multiple fronts.

72 # Introduction

73 In the five years since COVID-19 was first identified, Severe Acute Respiratory Syndrome Coronavirus
74 2 (SARS-CoV-2) has caused an estimated 776 million human infections and 7 million deaths worldwide
75 [1]. The fast roll-out of innovative vaccines was crucial in addressing the global health crisis when SARS-
76 CoV-2 suddenly emerged in the human population. Today, annual COVID-19 vaccination remains
77 recommended, as the vaccines provide only short-term immunity and the virus continues to undergo
78 antigenic drift. Serious complications from COVID-19 are common in vulnerable individuals, such as the
79 elderly or immunocompromised patients. For those with mild-to-moderate COVID-19 who are at high
80 risk for progression to severe disease, antiviral medication is recommended, specifically ritonavir-
81 boosted nirmatrelvir [which targets the coronavirus main protease (M^{pro})] or remdesivir [a nucleotide
82 inhibitor of the viral RNA-dependent RNA polymerase (RdRp)] [2].

83 To prepare for future outbreaks caused by drug-resistant variants or novel zoonotic coronaviruses
84 (CoVs), exploring alternative antiviral drug targets is essential. Many ongoing efforts are focused on one
85 of the 16 non-structural proteins (nsps) that make up the viral RNA transcription-replication complex
86 (RTC) [3-5]. Several nsps help the virus to evade the host innate immune response that aims to halt
87 viral replication [6]. This dual function also applies to nsp15, a uridine-specific endoribonuclease
88 (EndoU) that is highly conserved among all CoVs [7, 8]. As part of the RTC, nsp15 is believed to cleave
89 specific sites in viral RNA to regulate viral RNA synthesis [9]. Additionally, EndoU prevents the
90 accumulation of viral dsRNA intermediates, thereby avoiding their detection by dsRNA sensors of the
91 innate immune response [10-12]. This may be accomplished by EndoU cleavage of the 5´-poly(U)
92 extension in viral negative-sense RNA [12] or the CACA sequence near the 3´-poly(A) tail of the positive
93 strand [9]. Evidence also suggests that nsp15 interacts with cellular proteins involved in the production
94 of type I interferon (IFN-I) [13, 14] and may protect infected cells against apoptosis [10, 15], autophagy
95 [16], cell cycle arrest [17] or the formation of stress granules [18-20].

96 The immune-evading activity of EndoU has been demonstrated in cell culture studies with different CoVs
97 [10, 11, 21, 22], including human nasal epithelial cells infected with SARS-CoV-2 [23]. EndoU-deficient
98 mutants of mouse hepatitis virus (MHV) and porcine epidemic diarrhea virus (PEDV) proved significantly
99 less pathogenic than their wild-type (WT) counterparts in mice and piglets, respectively [10, 21].

100 However, an EndoU-deficient mutant of transmissible gastroenteritis virus exhibited comparable
101 virulence to WT in piglets, while the analogous mutant of feline infectious peritonitis virus was more
102 virulent than WT in cats [24]. Hence, many questions remain about the functions of EndoU in viral
103 replication and immune evasion.

104 The potential of nsp15 as a novel drug target has spurred recent efforts to identify inhibitors in enzymatic
105 EndoU assays [25-30] and resolve the protein structure of nsp15 in complex with a mono- or
106 oligonucleotide ligand [31-35]. For nearly all CoVs, including SARS-CoV-2, nsp15 adopts a
107 characteristic hexameric structure consisting of a dimer of trimers, with the six EndoU domains facing
108 outwards of the complex [36]. Each monomer contains an N-terminal domain (NTD), middle domain and
109 C-terminal domain harboring the EndoU site. Nsp15 hexamerization is regulated by the NTD and crucial
110 for EndoU enzymatic activity [37]. A recent review covers the biochemical properties, structure and
111 assumed functions of nsp15 in greater detail and can be found elsewhere [38].

112 Our interest in developing nsp15 inhibitors started several years ago, following the identification of a
113 betulonic acid-based inhibitor (encoded 5h in reference [39]) that exhibits submicromolar activity against
114 human coronavirus 229E (HCoV-229E), low cytotoxicity and a mechanism related to nsp15. The finding
115 that viral resistance to this compound was mapped to an inter-protomer region in the hexameric nsp15
116 protein of HCoV-229E, allowed us to create a docking model and predict the binding mode of 5h [39].
117 Shortly after, we identified compound EPB-113, another inhibitor of HCoV-229E that is structurally
118 unrelated to 5h. Intrigued by the discovery that viral resistance to EPB-113 was linked to mutations in
119 the catalytic center of nsp15 EndoU, we conducted the present study to uncover the mechanism of this
120 antiviral molecule. Through cell-based assays, we explored the association between EndoU and the
121 innate immune response, as well as other presumed functions of nsp15 beyond EndoU. We also
122 thoroughly profiled EPB-113-resistant nsp15-mutant viruses. Furthermore, biochemical assays with
123 recombinant nsp15 protein revealed that EPB-113 enhances the EndoU activity, which was opposite to
124 our initial expectations. Taking together, our findings suggest that EPB-113 acts through a previously
125 unrecognized pharmacological mechanism, by binding to nsp15, altering its conformation and disrupting
126 both its EndoU activity and other functions in viral replication and immune evasion.

127 # Materials and methods

128 ## Compounds

129 In S1 Appendix, we provide all details on the chemical synthesis, analysis and full characterization of
130 diphenylurea compounds EPB-113, EPB-102 and JMLV-061. The synthesis of 5h, a closely related
131 1,2,3-triazolo-fused betulonic acid derivatives, was described previously [39].
132 The following compounds were purchased from a commercial supplier: GS-441524 (Carbosynth); E64d
133 (MedChemExpress); nirmatrelvir (Chemat); and K22 (ChemDiv). Recombinant human IFN-β was
134 purchased from PeproTech.

135 ## Cells and media

136 Human embryonic lung fibroblast cells [HEL299; American Type Culture Collection (ATCC) No. CCL-
137 137] were cultured in Dulbecco's modified Eagle medium (DMEM) supplemented with 10% fetal calf
138 serum (FCS); 10 mM HEPES; 1 mM sodium pyruvate; 6 mM L-glutamine; 0.1 mM non-essential amino
139 acids (NEAA); and 25 mM glucose. For experiments, they were seeded on day -7 in 96-well plates and
140 grown until confluent, using DMEM with 2% FCS; 0.075% sodium bicarbonate; 1 mM sodium pyruvate;
141 0.1 mM NEAA; and pen-strep (= 100 U/ml penicillin and 0.1 mg/ml streptomycin). Human bronchial
142 epithelial 16HBE cells (kind gift from P. Hoet, KU Leuven) and BHK-21J cells (donated by P. J.
143 Bredenbeek) were maintained in DMEM with 10% FCS; 1 mM sodium pyruvate; 0.075% sodium
144 bicarbonate; 0.1 mM NEAA; 4 mM L-glutamine; and 25 mM glucose. For experiments, 16HBE cells were
145 seeded on day -1 in 96-well plates (30,000 cells per well), using the same medium but with 2% FCS and
146 pen-strep. A549 cells expressing ACE2 and TMPRSS2 ($A549^{ACE2/TMPRSS2}$) were purchased from
147 InvivoGen (No. a549d-cov2r) and cultured in DMEM supplemented with 6 mM L-glutamine; 25 mM
148 glucose; 10% FCS; 100 µg/ml hygromycin and 0.5 µg/ml puromycin. HEK-Blue IFN-α/β cells (kindly
149 donated by X. Saelens, UGent) were grown in DMEM with 4 mM L-glutamine; 25 mM glucose; 10%
150 heat-inactivated FCS; pen-strep; 30 µg/ml blasticidin; and 100 µg/ml zeocin.
151 Human macrophages were purified from healthy donor buffy coats, obtained from the Red Cross
152 Belgium according to KU Leuven agreement RKOV_19006. After isolating the mononuclear cell fraction
153 by density gradient centrifugation on Pancoll (PAN-Biotech), the monocytes were purified by adherence

154 for 1.5 h at 37 °C, followed by three PBS washes to remove non-adherent cells. The cells were seeded
155 in 96-well plates (90,000 cells per well) and allowed to differentiate into macrophages during six days
156 incubation in RPMI1640 medium with 2 mM glutamine and supplemented with 10% heat-inactivated
157 FCS; 2 mM L-alanyl-glutamine; 20 ng/ml macrophage-colony stimulating factor (M-CSF, PeproTech);
158 and pen-strep. Fresh medium was provided on day 3. For infection experiments, we used the same
159 medium but with 2% FCS.
160 All cells were incubated in a humidified 5% CO_2 incubator at 37 °C.

161 Viruses

162 HCoV-229E (ATCC No. VR-740) was expanded in HEL299 cells. Reverse-engineered HCoV-229E virus
163 carrying substitution $H250A_{nsp15}$ was kindly provided by V. Thiel (University of Bern). The SARS-CoV-2
164 viruses were created by reverse-engineering (see below). The stocks of wild-type and nsp15-mutant
165 viruses (see below) were titrated in HEL299 (for HCoV-229E) or $A549^{ACE2/TMPRSS2}$ cells (for SARS-CoV-
166 2) and the 50% cell culture infective dose ($CCID_{50}$) was calculated by the method of Reed and Muench.
167 All infection experiments were done at 35 °C for HCoV-229E and 37 °C for SARS-CoV-2.

168 Antiviral and cytotoxicity assays

169 Unless specified differently, the compounds' antiviral activity was determined in HEL299 cells infected
170 with HCoV-229E or in $A549^{ACE2/TMPRSS2}$ cells infected with SARS-CoV-2, both at a multiplicity of infection
171 (MOI) of 100 $CCID_{50}$. Serial dilutions of the compounds were added to the cells in 96-well plates,
172 immediately followed by the virus. A mock-infected plate was prepared in parallel, to assess compound
173 cytotoxicity. To study combinations, different concentrations of the two compounds were added in a
174 matrix of 8x8 wells. For the CPE reduction assay, the viral CPE was scored by microscopy at day 5 p.i.,
175 then quantified by the colorimetric MTS cell viability assay. After replacing the supernatant by CellTiter
176 $96AQ_{ueous}$ MTS Reagent (Promega) and incubating the plates for 24 h (HEL299) or 6 h
177 ($A549^{ACE2/TMPRSS2}$) at 37 °C, the A_{490} values were measured in a Tecan Spark 10M plate reader. To
178 calculate the EC_{50} (50% antivirally effective concentration) and CC_{50} (50% cytotoxic concentration)
179 values, we used the formulas specified elsewhere [40].
180 For virus yield reduction assays, the supernatants were harvested at day 3 to 5 p.i. To quantify the viral
181 load by RT-qPCR, the samples were mixed with Cells-to-cDNA II lysis buffer (Invitrogen) and incubated
182 for 10 min at 75 °C. The number of viral RNA genomes (= viral load) was determined by one-step RT-

183 qPCR (iTaq Universal Probes One-Step kit, BioRad), employing N-gene specific primers and probe (see
184 sequences provided in S2 Appendix) and an N-gene plasmid standard to allow absolute quantification
185 [41]. The RT-qPCR program consisted of: 10 min at 50 °C; 2 min at 95 °C; and 40 cycles of 15 s at 95
186 °C and 60 s at 60 °C. To quantify the yield of infectious virus, we incubated serial dilutions of the
187 supernatants with HEL299 cells in 96-well plates, scored the CPE at day 5 p.i. and calculated the $CCID_{50}$
188 titers as described above. Antiviral activity in these virus yield assays was expressed as the EC_{90} value,
189 i.e. compound concentration producing 1-log_{10} reduction in the number of viral RNA genomes or in the
190 $CCID_{50}$ titer. Compound cytotoxicity was assessed in parallel in mock-infected plates by MTS cell
191 viability assay at day 3 or 5 p.i.

192 Time-of-compound addition assay

193 Confluent HEL299 cells were infected with HCoV-229E and the compounds were added to separate
194 wells at -0.5, 0.5, 2, 4, 6, 8, 10, 12 or 14 h p.i. At 16 h p.i., the cells were washed with ice-cold PBS, then
195 lysed by adding Cells-to-cDNA II lysis buffer and incubating for 10 min at 75 °C. The viral RNA copy
196 number in each sample was determined by one-step RT-qPCR as explained above. The starting number
197 of viral RNA copies (= input RNA) was determined in a cell lysate (from the no compound condition)
198 made at 2 h p.i.

199 Selection of compound-resistant HCoV-229E viruses

200 Instead of performing serial virus passaging, we used a faster resistance selection method (that was
201 earlier developed for Chikungunya virus by Delang et al. [42]. First, HEL299 cells were exposed to serial
202 dilutions of HCoV-229E and compound (EPB-113 or JMLv-061). At day 4 p.i., the optimal condition for
203 resistance selection was defined as the condition receiving the highest MOI and lowest compound
204 concentration achieving complete prevention of CPE. Subsequently, this virus/compound condition was
205 applied to all wells of a 96-well plate with HEL299 cells. At day 4 p.i., the CPE was scored by microscopy
206 and the wells showing virus breakthrough were selected to harvest supernatants and expand the
207 progeny virus. For virus sequencing, we prepared RNA extracts from the expanded virus stocks
208 (QIAamp Viral RNA Kit; Qiagen) and performed high-fidelity RT-PCR (SuperScript IV One-Step RT-PCR
209 System; Invitrogen), yielding five overlapping cDNA fragments that covered the entire viral genome.
210 After Sanger sequencing (Macrogen Europe) with a set of 39 primers, the mutations selected under
211 EPB-113 or JMLv-061 were identified by aligning the sequences of compound-selected and wild-type

212 (WT) forms of HCoV-229E, using CLC Main Workbench (Qiagen). To conduct antiviral experiments, the
213 mutant viruses were plaque-purified in HEL299 cells grown in 6-well plates in the presence of 20 µM
214 compound and overlaid with 0.4% UltraPure Low Melting Point Agarose (Invitrogen).

215 Reverse-engineering on SARS-CoV-2

216 Starting from seven reverse genetics plasmids which were generously donated by P.-Y. Shi (World
217 Reference Center for Emerging Viruses and Arboviruses, Texas) [43], we first replaced their sequences
218 encoding SARS-CoV-2 strain SARS-CoV-2/USA_WA1/2020 by the analogous sequences of Omicron
219 subvariant BF.7. Therefore, viral RNA was extracted (QIAamp viral RNA kit, Qiagen) from a clinical
220 isolate (pango lineage BF.7; hCoV-19/Belgium/rega-43668/2022; EPI_ISL_14623620), followed by
221 reverse transcription (Superscript IV RT First-Strand synthesis system, Invitrogen) and PCR (Platinum
222 SuperFi PCR, Invitrogen). The resulting fragments were used to replace the WA1-sequences in the
223 seven reverse genetics plasmids (NEBuilder HiFi DNA Assembly Cloning Kit, New England Biolabs).
224 For generating mutants, site-directed mutagenesis was performed with overlapping mutagenic primers
225 and Platinum SuperFi II DNA Polymerase (Invitrogen). The procedure for reverse-engineering SARS-
226 CoV-2 was adapted from Xie et al [43]. The plasmids were transformed into One Shot TOP10 Chemically
227 Competent *E. coli* (Invitrogen; for pUC57-based plasmids) or TransforMax EPI300 *E. coli* (LGC
228 Biosearch Technologies; for pCC1-based plasmids) and purified with the Qiagen Plasmid Plus Maxi Kit.
229 All plasmids were validated by Sanger sequencing (Macrogen Europe). Next, SARS-CoV-2 DNA
230 fragments were recovered through restriction enzyme digestion of the seven plasmids and the
231 subsequent ligation step yielded full-length viral DNA. N-gene cDNA was prepared from the plasmid
232 containing the last part of the viral DNA via PCR (Platinum SuperFI II, Invitrogen). Using T7 polymerase
233 (mMESSAGE mMACHINE T7 transcription kit; Invitrogen), the full-length and N-gene viral DNA were *in*
234 *vitro* transcribed to obtain genomic and N-coding SARS-CoV-2 RNA, followed by purification by
235 phenol:chloroform extraction and isopropanol precipitation. Twenty µg of each was subsequently
236 electroporated into 8 million BHK-21J cells resuspended in PBS, using the Gene Pulser Xcell
237 Electroporation System (Bio-Rad). The electroporated cells were then seeded in a 75-cm² flask with
238 $A549^{ACE2\text{-}TMPRSS2}$ cells. The supernatants were harvested after three days, and further expanded in
239 $A549^{ACE2\text{-}TMPRSS2}$ cells. The resulting virus stocks were first subjected to nsp15 sequencing, with the
240 primers described by Xie et al. [43], to ensure that the desired mutations were present.

241 # HCoV-229E replication kinetics and expression of innate
242 immune factors

243 HEL299 cells, 16HBE cells and human macrophages were infected with WT or nsp15-mutant HCoV-
244 229E and 2 h later, the inoculum was replaced by fresh medium. At 2, 24, 48 and 72 h p.i., supernatant
245 samples were collected and the cells were extracted for total RNA (ReliaPrep RNA miniprep system,
246 Promega). The supernatants were analyzed for number of viral RNA genomes, using the one-step RT-
247 qPCR method from above, as well as for bioactive IFN-α/β (see below). To measure the mRNA levels
248 for a selection of innate immune factors, the cellular RNA extracts were submitted to RT-qPCR (High-
249 Capacity cDNA Reverse Transcription Kit, Applied Biosystems), using random primers for cDNA
250 synthesis and gene-specific primers (primer sequences are listed in S3 table) for qPCR (GoTaq qPCR
251 kit, Promega). The transcript levels for innate immune factors were normalized to the geometric mean
252 of those for the housekeeping genes ACTB and HPRT (ΔC_T) and the fold change was calculated as
253 $2^{-\Delta\Delta CT}$ over mock (ΔC_T target - ΔC_T mock).
254 The levels of bioactive IFN-α/β in the supernatants were quantified in HEK-blue IFN-α/β reporter cells,
255 following the manufacturer's instructions. In brief, 20 µl supernatant was added to the wells of a 96-well
256 plate and the reporter cells were added at 50,000 cells in a volume of 180 µl. Recombinant human IFN-β
257 was included as a positive control. After overnight incubation at 37 °C, 20-µl supernatant samples were
258 collected from the reporter cells, then combined with 180 µl QUANTI-blue solution (InvivoGen) in a 96-
259 well plate and incubated for 2 h at 37 °C. The A_{620} values were measured in a Tecan Spark 10M plate
260 reader. For calculations, all absorbance values were first adjusted by subtracting the blank, i.e. QUANTI-
261 blue in the corresponding medium per cell line, then expressed as the fold increase for virus- versus
262 mock-infected cells.

263 # Competitive fitness of nsp15 inhibitor-resistant viruses

264 HEL299 cells were co-infected with WT and nsp15-mutant HCoV-229E virus, mixed at a ratio of 9:1, 1:1
265 or 1:9. After three days incubation at 35 °C, the supernatants were harvested, titrated and applied to
266 fresh HEL299 cells. This procedure was repeated for an extra three passages. The supernatants of each
267 passage were collected for RNA extraction (QIAamp Viral RNA Kit, Qiagen) followed by RT-PCR
268 (SuperScript IV One-Step RT-PCR, Invitrogen) with primers 229E-For17743 and 229E-Rev24484

269 (sequences provided in S3 Table), resulting in ~6.7 kb amplicons covering the nsp15 gene. All PCR
270 products were sequenced using Oxford Nanopore Technologies devices. For passages 1 and 2, library
271 preparation was performed using the SQK-RBK110.96 kit and sequencing was done on an r9.4.1 flow
272 cell connected to a GridION (MinKNOW v23.04.6; super-accurate basecalling). For passages 3 and 4,
273 library preparation was done using the SQK-NBD114.96 kit and the resulting library was sequenced on
274 an r10.4.1 PromethION flow cell using a P2 Solo device connected to a GridION (MinKNOW v23.07.12;
275 super-accurate basecalling). Filtlong (v0.2.1) was used to subset for each barcode the 10% highest
276 quality reads with a length between 6.5 and 7 kb. These subsets were mapped against the HCoV-229E
277 reference sequence (NC_002645.1) using the minimap2 (v2.24) map-ont preset [44], resulting in a
278 minimal coverage of 1200X at each site. Detailed coverage statistics per position were determined using
279 bam-readcount (v1.0.1), after which a custom bash script was used to calculate simplified percentages
280 of WT and nsp-15 mutant motif prevalence at each virus passage [45].

281 Production of recombinant nsp15 protein from HCoV-229E
282 and SARS-CoV-2

283 The pET28a(+) plasmid for bacterial expression of SARS-CoV-2 nsp15 was a kind gift from B. Canard
284 (Aix-Marseille University). To engineer the corresponding plasmid for HCoV-229E nsp15, the sequence
285 (codon-optimized for expression in *E. coli*) was supplemented with an N-terminal octahistidine tag and
286 TEV cleavage site and ordered as a gBlock from IDT. This DNA was cloned in the pET28a(+) vector
287 using the NEBuilder HiFi DNA assembly cloning kit (NEB) and corresponding instructions. To produce
288 the two proteins, T7 Express Competent *E. coli* cells (NEB) were transformed with pET28a(+)-nsp15
289 plasmid, as instructed by the supplier. A starter culture was grown overnight in 100 ml Luria–Bertani (LB)
290 broth with 50 µg/ml kanamycin, using a shaking incubator (100 rpm) at 37 °C. From this, 10 ml was
291 added to 1 liter LB medium with 50 µg/ml kanamycin, and the bacteria were grown until an OD_{600} of ~0.6
292 was reached. Protein expression was induced at 500 µM isopropyl β-D-1-thiogalactopyranoside, and
293 the cultures were incubated overnight at 18 °C, after which the cells were pelleted by centrifugation (30
294 min, 5000 g, 4 °C) and stored at -20 °C. For protein purification, the pellets were resuspended in lysis
295 buffer (50 mM Tris pH 8; 300 mM NaCl; 20 mM imidazole; and 1 mM dithiothreitol (DTT), supplemented
296 with 1 mM phenylmethylsulfonyl fluoride, 1% Triton-X, 30 mg lysozyme, 20 mM MgSO4, 100 U DNase
297 I). After cell disruption by high pressure using EmulsiFlex-C3 (Avestin), 4 times at 20,000 bar, cell debris

298 was removed by centrifugation (40 min, 5000 x g, 4 °C) and filtration through a 0.45 µm Whatman GD/XP
299 Syringe Filter (Cytiva). The filtered lysates were subjected to Ni-NTA chromatography (Qiagen)
300 equilibrated with the lysis buffer without supplement, washed and eluted with the increasing
301 concentration of the imidazole (20-300 mM Imidazole). The eluted protein is then applied to a HiLoad
302 Superdex 16/600 200 pg size-exclusion chromatography (SEC) column (GE Healthcare) and run in a
303 buffer containing 25 mM HEPES at pH 8, 300 mM NaCl, 10% glycerol, and 1 mM tris(2-
304 carboxyethyl)phosphine. Finally, the protein solutions were concentrated with a centricon (VivaSpin 15R
305 centricon, 10,000 MWCO; Sartorius AG). The protein products were analyzed by dynamic light
306 scattering (DLS; S1 Fig), which showed that the nsp15 proteins were ≥ 98% pure and present in
307 hexameric form, in line with other reports [46, 47].

308 Biophysical evaluation of the compound-nsp15 interaction

309 The thermal shift assay was executed in white PCR plates. The wells contained 6 µM nsp15 (diluted in
310 assay buffer: 20 mM HEPES pH 7.5; 50 mM NaCl; 5 mM $MnCl_2$; and 1 mM DTT), 5x SYPRO orange
311 dye and either 100 µM test compound or the corresponding percentage of DMSO. Using a QuantStudio
312 5 Real-Time PCR system (Thermo Fisher), fluorescence was continuously monitored while the plate
313 was heated from 4 to 95 °C at a ramp rate of 0.05 °C/s. The nsp15 melting temperature (T_m) was
314 calculated by determining the temperature at which the negative first derivative of the fluorescence
315 versus temperature (-dFluorescence/dT) reaches its minimum, using Protein Thermal Shift Software
316 v1.3 (Thermo Fisher).

317 To assess the interaction between EPB-113 and nsp15 from SARS-CoV-2 or HCoV-229E by surface
318 plasmon resonance (SPR), we used a Biacore 8K instrument (Cytiva). Nsp15 was covalently coupled
319 onto a CM4 sensor chip (Cytiva) at a density of around 3500 resonance units (RU) using standard amine
320 coupling chemistry in 10 mM acetate buffer pH 5.5. A reference flow was used as a control for non-
321 specific binding and refractive index changes. All binding experiments were performed at 25 °C in 50
322 mM Tris buffer supplemented with 500 mM NaCl, 5 mM $MnCl_2$, 0.05% Tween20 and 5% DMSO. Serial
323 dilutions of EPB-113 or EPB-102 were injected for 120 s at a flow rate of 30 µl/min. The dissociation was
324 monitored for 6 min. Buffer blanks were used for double referencing and a DMSO solvent correction
325 was included. Biacore Insight Software 5.0.18 was used for analysis.

326

327 # Enzymatic EndoU assay

328 For the FRET-based EndoU cleavage assay, we employed a 5-nt single-stranded DNA-RNA hybrid
329 substrate (5′-6-FAM-AArUAA-3′-IABkFQ; synthesized by IDT), that contained a single U↓A-cleavage
330 site, 5′-carboxyfluorescein (FAM) fluorophore and 3′-Iowa Black quencher [27]. The assay was
331 conducted in black half-area 96-well plates, using the same assay buffer as in the thermal shift assay.
332 The wells (25 µl total volume) contained 63 nM (HCoV-229E) or 4 nM (SARS-CoV-2) nsp15, 0.5 µM
333 substrate and 100 µM of compound or the corresponding percentage of DMSO. Using a Tecan Spark
334 10M plate reader set at 485 nm emission and 535 nm excitation wavelength, the increasing fluorescence
335 was continuously measured during 1 h at 37 °C. The initial cleavage rate (V_0) was obtained by
336 calculating the slope (RFU/s) of the 5-10 min time interval of the cleavage reaction.

337 In parallel, the samples after 1 h reaction time were analyzed by HPLC on a capillary chromatography
338 instrument (CapLC, Waters) equipped with a C18 reversed-phase column (PepMap 0.5 x 15 mm, LC
339 Packings). The elution buffer contained 0.05% v/v *N,N*-dimethylaminobutane (DMAB, Acros) as ion
340 pairing reagent and 1% v/v 1,1,1,3,3,3-hexafluoro-2-propanol (hexafluoroisopropanol, HFiP, Acros) in
341 water (pH 8.0). The organic phase consisted of 50% v/v acetonitrile (Fisher Scientific) in water.
342 Oligonucleotides were eluted at a flow rate of 12 µl per min, applying a gradient starting at 5% organic
343 phase and increasing by 20% per min during 4 min. The mass spectrometer consisted of a quadrupole
344 time-of-flight instrument (Synapt G2 HDMS, Waters) equipped with a standard electrospray source.
345 Every 2 s, spectra were recorded in negative ion mode with following settings: cone voltage 35 V,
346 capillary voltage 2200 V, source temperature 80 °C and N_2 desolvation gas 600 L/h. The acquired
347 spectra were mass corrected using leucine enkephalin and deconvoluted applying the MaxEnt algorithm
348 (MassLynx 4.1, Waters).

349 # Data analysis and statistics

350 All graphs were created with GraphPad Prism 10.3.1 software, which was also used for statistical
351 analysis. Statistical significance is shown as: ****$P \leq 0.0001$, ***$P \leq 0.001$, **$P \leq 0.01$, *$P \leq 0.05$, ns: not
352 significant.

Results

EPB-113 is a strong replication inhibitor of HCoV-229E that also suppresses SARS-CoV-2

HCoV-229E differs from other human CoVs in causing manifest cytopathic effect (CPE) in different cell lines, while its manipulation is allowed at biosafety level 2. Based on this, we have been using since several years a CPE reduction assay in HCoV-229E-infected HEL299 cells, to conduct convenient phenotypic screening for novel CoV inhibitors. To assess the compounds' antiviral effect, the viral CPE is quantified by MTS cell viability assay in combination with microscopic examination. These two methods are also used to determine compound cytotoxicity in mock-infected cells.

Our screening campaign identified compound EPB-113 as a robust lead compound, exhibiting an EC_{50} value for HCoV-229E of 0.48 µM and CC_{50} value for HEL299 cells of 92 µM, thus yielding a favorable selectivity index (SI; ratio of CC_{50} to EC_{50}) of 193 (Figs 1B and 1D). Antiviral activity was very similar whether determined by MTS assay or by microscopic scoring (Fig 1D). The activity was confirmed when we quantified the virus in the supernatant at day 3 p.i. Here, EPB-113 showed an EC_{90} value of 0.65 µM based on RT-qPCR for viral genome copies and of 0.40 µM based on titration of infectious virus (Figs 1B and 1D). In HCoV-229E-infected HEL299 cells, EPB-113 outperformed GS-441524, the nucleoside form of remdesivir that was included as reference compound [EC_{50} value of 3.5 µM (CPE assay) and EC_{90} value of 2.5 and 4.6 µM (by infectious virus titration and RT-qPCR, respectively)].

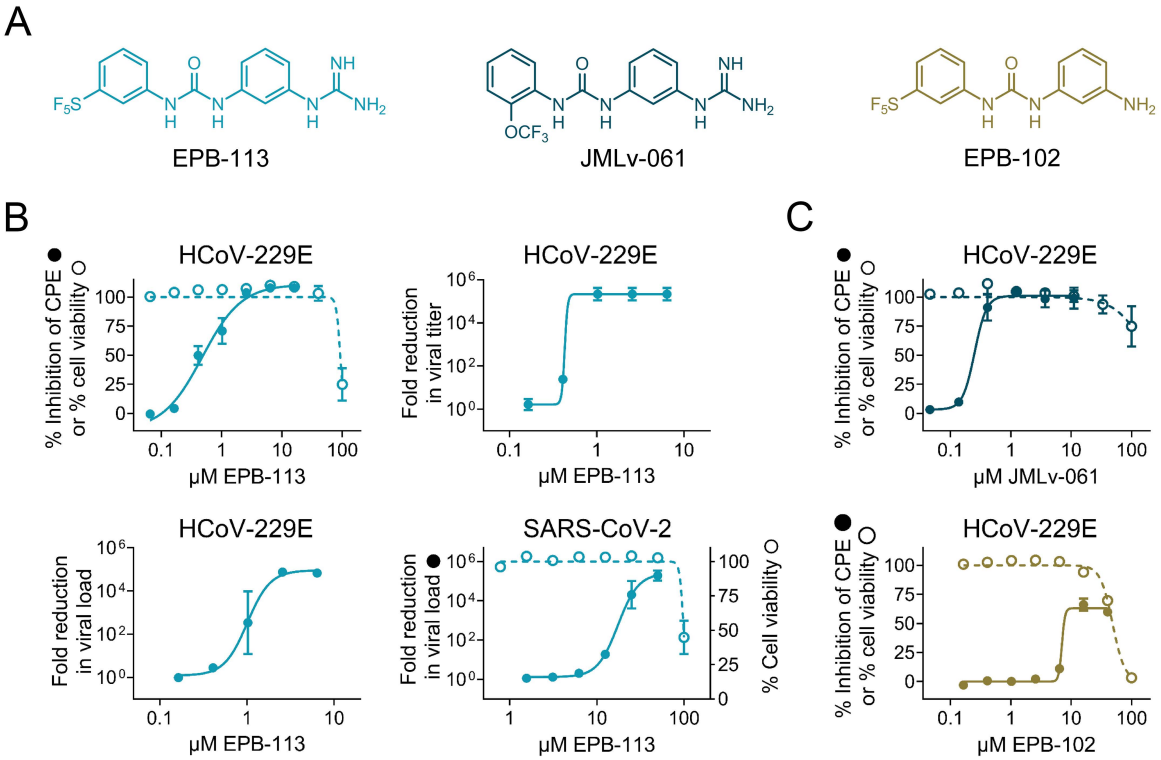

D

Compound	Virus	Antiviral activity				Cytotoxicity
		EC_{50} (CPE)	EC_{50} (MTS)	EC_{90} (infectious titer)	EC_{90} (viral load)	CC_{50}
EPB-113	HCoV-229E	1.0	0.48	0.40	0.65	92
	SARS-CoV-2	12	-	-	12	99
JMLv-061	HCoV-229E	0.33	0.25	-	-	> 100
EPB-102	HCoV-229E	12	7.0	-	-	48
GS-441524	HCoV-229E	3.5	2.6	2.5	4.6	> 100
	SARS-CoV-2	1.3	-	-	1.7	> 25

Fig 1. Inhibitory activity of EPB-113 on the replication of HCoV-229E and SARS-CoV-2. (A) Chemical structures of EPB-113 and its structural analogues EPB-102 and JMLv-061. (B) Inhibition of HCoV-229E replication in HEL299 cells was determined by MTS-based CPE reduction assay; infectious virus titration on the supernatant; and RT-qPCR-based viral load assay. Inhibition of SARS-CoV-2 replication in $A549^{ACE2/TMPRSS2}$ cells was quantified by viral load assay. Cytotoxicity was determined by MTS cell viability assay in mock-infected cells and is shown in dashed lines (open circles). Data points are the mean ± SEM (N=3-12). (C) Anti-HCoV-229E activity and cytotoxicity in HEL299 cells for EPB-102 and JMLv-061, two structural analogues of EPB-113. Data points are the mean ± SEM (N=3). (D) Table summarizing the values for antiviral activity and cytotoxicity of EPB-113, JMLv-061, EPB-102 and reference compound GS-441524.

382 Chemically, EPB-113 is a diphenylurea compound featuring a *m*-guanidine function in an aromatic ring
383 and a *m*-pentafluorosulfanyl group in the other aromatic ring (Fig 1A). To determine the structure-activity
384 relationship for HCoV-229E, we synthesized a series of more than 20 structural analogues, the outcome
385 of which will be published in a separate report (S. Vazquez, manuscript in preparation). Of note, as the
386 very lipophilic *m*-pentafluorosulfanyl group is uncommon in medicinal chemistry, we also evaluated other
387 analogs lacking this group, such as JMLv-061 (Fig 1A), with an *o*-trifluoromethoxy group instead of the
388 *m*-pentafluorosulfanyl unit, but keeping the *m*-guanidine group on the other aromatic ring. While this
389 change had no impact on the antiviral activity (EC_{50} for JMLv-061: 0.33 µM in HCoV-229E infected
390 HEL299 cells; Figs 1C and 1D), the analog lacking the guanidine function (= EPB-102; Fig 1A) was
391 shown to have much weaker activity (EC_{50} of 12 µM in HCoV-229E infected HEL299 cells, reaching only
392 60% inhibition at 40 µM; Figs 1C and 1D), thus highlighting the relevance of the guanidine group in the
393 antiviral activity.

394 EPB-113 proved also a robust inhibitor of SARS-CoV-2 replication in $A549^{ACE2\text{-}TMPRSS2}$ cells. The
395 molecule was shown to have an EC_{90} value (by RT-qPCR for viral load) of 12 µM and to produce more
396 than 5-log_{10} reduction in viral load at 50 µM of compound (Fig 1B). The cell viability of mock-infected
397 $A549^{ACE2\text{-}TMPRSS2}$ cells was 100% at 50 µM EPB-113 and 45% at 100 µM compound (Fig 1B), which is
398 similar to what was seen in HEL299 cells.

399

400 Viral resistance to EPB-113 maps to the catalytic core of
401 nsp15 EndoU

402 To identify the target of EPB-113, we performed selection of resistant virus. For this and all subsequent
403 mechanistic experiments, we chose to use HCoV-229E instead of SARS-CoV-2, since this allowed to
404 apply the compound at a concentration that was well above the EC_{50} value. In the first step (Fig 2A), we
405 determined the optimal condition, being the highest MOI of HCoV-229E and lowest compound
406 concentration for which viral CPE was completely inhibited. Next, we applied this condition (i.e. 20 µM
407 of compound) to all wells of a 96-well plate with HEL299 cells. To maximize the chances of obtaining
408 resistance, we added EPB-113 to one plate and its analogue JMLv-061 to a second plate. At day 4 p.i.,

409 the few wells showing virus breakthrough were selected for virus expansion and subsequent full-genome

410 sequencing.

411

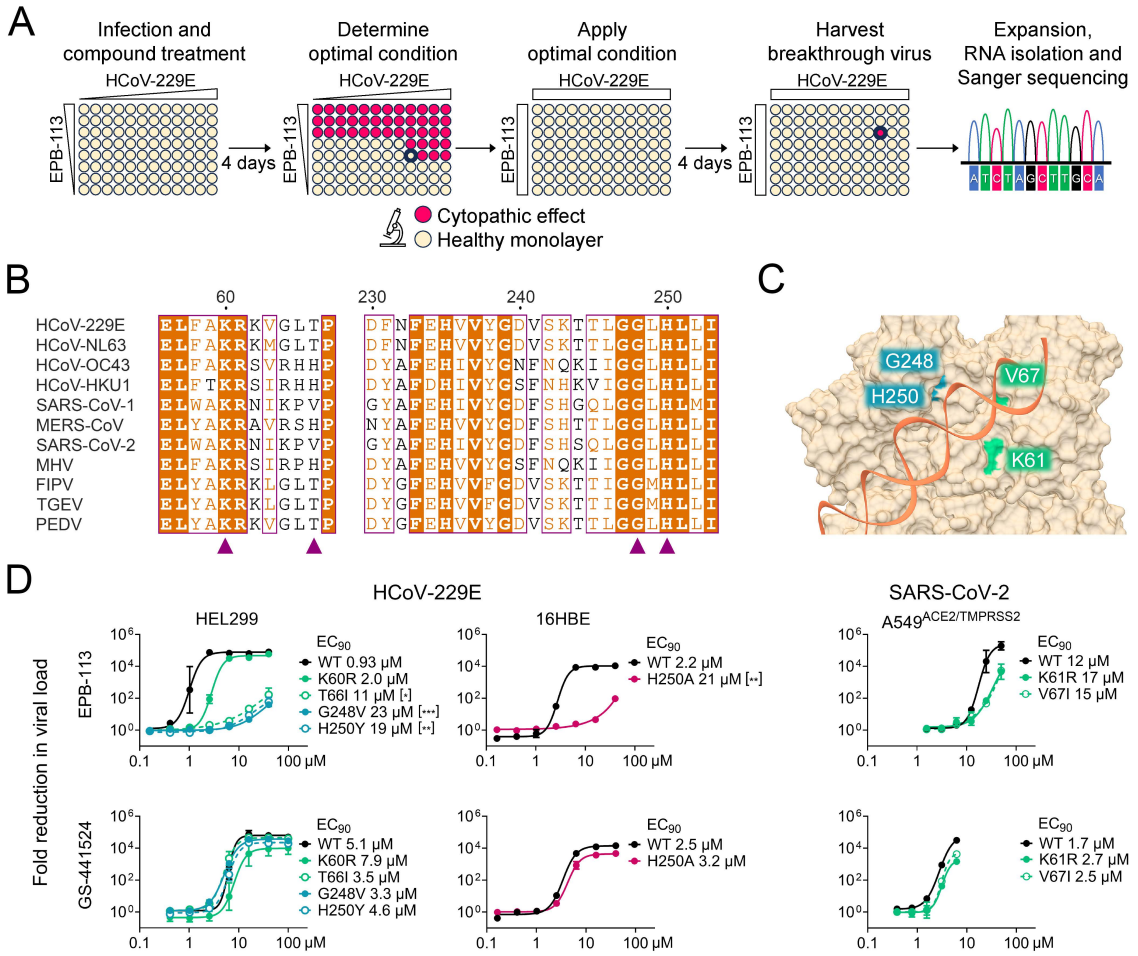

412

413 **Fig 2. Resistance to EPB-113 maps to the catalytic core of nsp15 EndoU.** (A) Setup of the resistance selection

414 experiment. (B) Alignment of partial nsp15 sequences from 11 coronaviruses, with EPB-113 and 5h resistance sites

415 marked with triangles. Both EPB-113 resistance sites, G248 and H250, are located at the catalytic core of nsp15

416 EndoU and strictly conserved in all CoVs, with H250 being part of the catalytic triad. Sequence similarities from

417 Clustal Omega-aligned sequences were rendered using ESPript 3.0. (C) Structure of the catalytic core of SARS-

418 CoV-2 EndoU bound to dsRNA (PDB 7TJ2). The residues associated with HCoV-229E resistance to EPB-113 or 5h

419 [39] are marked in blue and green, respectively. (D) Evaluation of EPB-113 and reference compound GS-441524

420 against nsp15-mutant CoVs, based on RT-qPCR-based viral load assay. Left panels: HEL299 cells infected with

421 HCoV-229E WT; the G248V$_{nsp15}$ or H250Y$_{nsp15}$ mutant (obtained in this study); or the K60R$_{nsp15}$ or T66$_{nsp15}$ mutant

422 (previously selected under compound 5h) [39]. Middle panels: 16HBE cells infected with H250A$_{nsp15}$ mutant HCoV-

423 229E, created by reverse genetics [11]. Right panels: A549$^{ACE2/TMPRSS2}$ cells infected with K61R$_{nsp15}$ or V67I$_{nsp15}$

424 mutant SARS-CoV-2, created by reverse genetics. Data points are the mean ± SEM (N=2-3). The panel legends
425 show the EC_{90} values and statistical significance of the difference between mutant and WT, based on (left panels)
426 ordinary one-way ANOVA with Dunnett's corrections for multiple comparisons and (middle panels) two-tailed
427 unpaired t-test.

428

429 The breakthrough viruses were found to carry mutations G248V and H250Y in the EndoU domain of
430 nsp15, after selection under EPB-113 and JMLv-061, respectively. After obtaining plaque-purified mutant
431 viruses, we confirmed their resistance by RT-qPCR-based viral load assay in which the increase in EC_{90}
432 value between mutant and WT was 20- to 25-fold (Fig 2D). Also another variant at the His250 site, i.e.
433 the $H250A_{nsp15}$ mutant form of HCoV-229E which was created by the V. Thiel team using reverse-
434 engineering [11], proved to be highly resistant to EPB-113 (Fig 2D). In this case the assay was done in
435 16HBE cells, since the $H250A_{nsp15}$ virus showed significantly impaired replication in HEL299 cells (see
436 below). The reference compound GS-441524 was equally active against the nsp15-mutant viruses and
437 WT.

438 Residues Gly248 and His250 are strictly conserved among CoVs and located in the catalytic center of
439 EndoU (Figs 2B and 2C). While His250 is part of the catalytic triad, the nearby Gly248 residue was
440 reported to engage in hydrogen bonding with the 3′-phosphate of the cleavage product [33].

441 As mentioned in the introduction, our group previously [39] identified betulonic acid derivative 5h as a
442 strong inhibitor of HCoV-229E which selects for resistance mutations $K60R_{nsp15}$ and $T66I_{nsp15}$ near the
443 EndoU catalytic core (Fig 2C). Considering that EPB-113 and 5h have totally different chemical
444 structures, we investigated whether the two compounds are synergistic when combined. Data analysis
445 with the zero-interaction potency (ZIP) model in SynergyFinder+ (S2 Fig) [48] indicated that the
446 combination of EPB-113 and 5h is synergistic (mean ZIP synergy score: 12), suggesting that these two
447 inhibitors possess non-overlapping mechanisms that potentiate each other. The combinations of EPB-
448 113 plus GS-441524 or 5h plus GS-441524 proved additive (mean ZIP synergy score below 10 in both
449 cases).

450 We next investigated potential cross-resistance between the two inhibitor classes. For this experiment
451 we used mutant viruses $T66I_{nsp15}$ and $K60R_{nsp15}$, which arose after virus passaging under 5h [39]. Fig
452 2D shows that the activity of EPB-113 was strongly affected by $T66I_{nsp15}$, the shift in EC_{90} value versus

453 WT virus being almost equally pronounced (12-fold) as for G248V$_{nsp15}$ and H250Y$_{nsp15}$. There was also
454 a 2-fold, yet non-significant, shift for the K60R$_{nsp15}$ mutant.

455 To assess whether the above resistance profile of HCoV-229E also applies to SARS-CoV-2, reverse
456 engineering was performed to introduce the above mutations in SARS-CoV-2. We were unable to rescue
457 SARS-CoV-2 virus carrying substitution G248V$_{nsp15}$, H250Y$_{nsp15}$ or H250A$_{nsp15}$. Although this observation
458 underscores the importance of a functional EndoU during SARS-CoV-2 replication, we did not expect it,
459 as all three mutations proved clearly viable in the context of HCoV-229E. On the other hand, we
460 successfully generated the K61R$_{nsp15}$ and V67I$_{nsp15}$ mutants of SARS-CoV-2 (corresponding to K60R$_{nsp15}$
461 and V66I$_{nsp15}$ in HCoV-229E), and both viruses proved to be less sensitive to EPB-113 than WT virus
462 (Fig 2D, right panels).

463 In short, resistance selection with HCoV-229E, combined with reverse engineering on SARS-CoV-2,
464 showed that the antiviral effect of EPB-113 is tightly linked with nsp15, and specifically its EndoU domain.

465

466 EPB-113-resistant mutants of HCoV-229E have a replication 467 deficit

468 Attenuation in human macrophages

469 Since the nsp15 mutations causing reduced sensitivity to EPB-113 are located at (i.e. G248V$_{nsp15}$ and
470 H250Y$_{nsp15}$) or close to (i.e. K60R$_{nsp15}$ and T66I$_{nsp15}$) the EndoU catalytic core, we presumed that they
471 may impair the replication fitness of HCoV-229E. To thoroughly profile these mutants, we compared
472 them to WT virus as well as to the reverse-engineered H250A$_{nsp15}$ virus. The latter was previously
473 reported to be severely attenuated in human macrophages, due to early induction of IFN-I [11]. Hence,
474 we compared viral growth in human blood-derived macrophages, HEL299 human fibroblast cells (in
475 which our mutants arose under selective pressure of EPB-113 or 5h) and 16HBE human bronchial
476 epithelial cells.

477 In macrophages, no viral replication was detected for the G248V$_{nsp15}$, H250Y$_{nsp15}$ and H250A$_{nsp15}$
478 mutants (Fig 3A, left panels). The K60R$_{nsp15}$ and T66I$_{nsp15}$ mutants showed some growth impairment at
479 48 h and 72 h (3- to 17-fold reduction vs WT) but this was not significant. In 16HBE cells (Fig 3A, right

480 panels, most viruses showed very similar growth kinetics as WT virus, with only $G248V_{nsp15}$, $H250Y_{nsp15}$
481 and $H250A_{nsp15}$ showing a slight (3- to 8-fold) reduction at 48-72 h, which was only significant for
482 $H250Y_{nsp15}$ and $H250A_{nsp15}$ ($P \leq 0.05$ at 48 h). An intermediate picture was seen in HEL cells (Fig 3A,
483 middle panels). Here, the $H250Y_{nsp15}$ and $H250A_{nsp15}$ mutants were significantly impaired (7- to 56-fold;
484 $P \leq 0.01$) at 24 to 72 h p.i. The $G248V_{nsp15}$ and $K60R_{nsp15}$ mutants showed a modest (4- to 7-fold)
485 reduction, while the $T66I_{nsp15}$ virus was indistinguishable from WT virus.

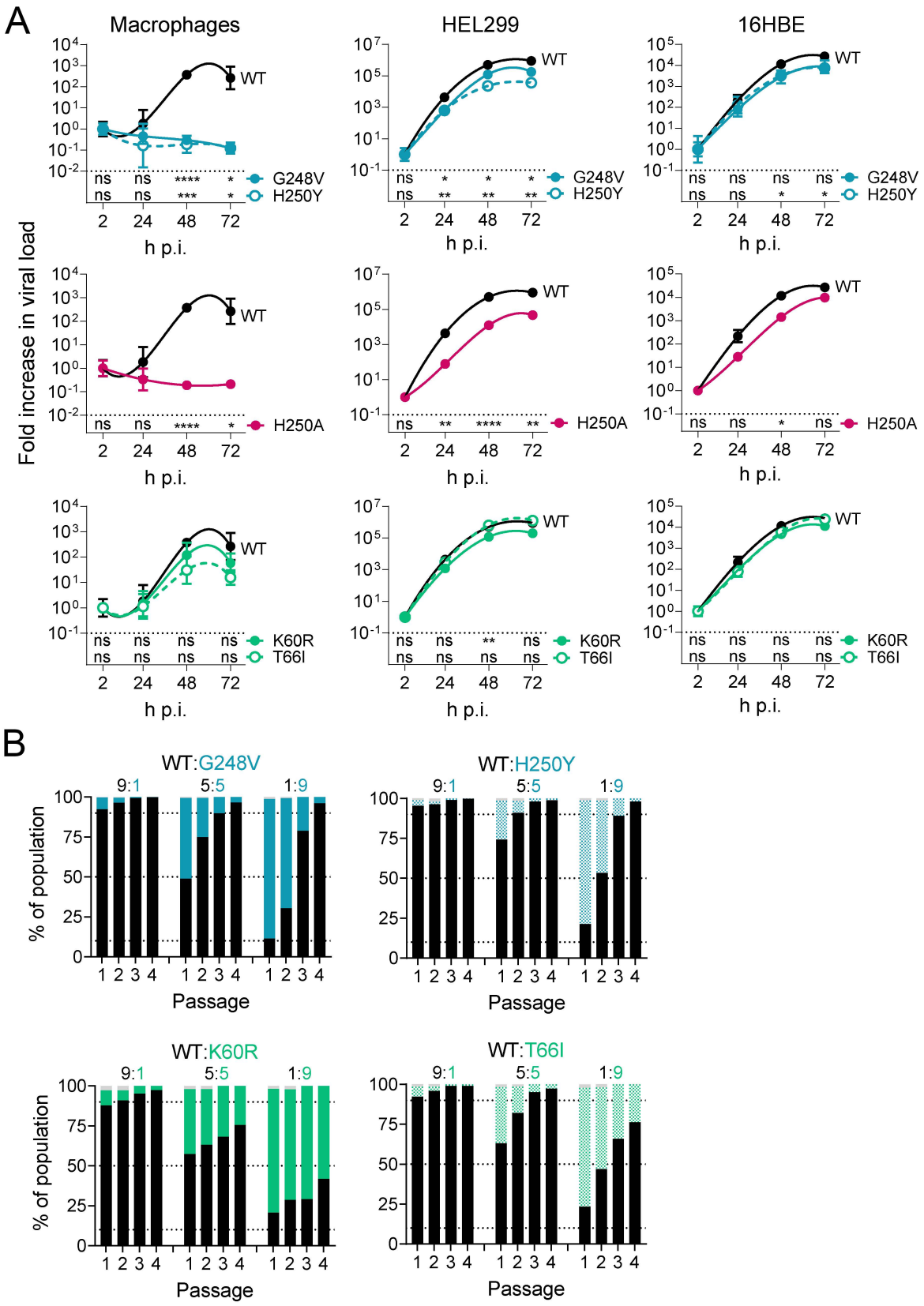

Fig 3. HCoV-229E viruses bearing EPB-113 resistance mutations have impaired viral fitness. (A) Replication kinetics in human macrophages, HEL299 cells and 16HBE cells, based on RT-qPCR for viral load. Data points are the mean ± SEM (N=3). At each time point, statistical significance is shown for the difference between mutant and

490 WT (multiple unpaired t-tests, with Holm-Šídák's correction for multiple comparisons). (B) Competitive growth assay.
491 At the start of the experiment, each mutant was mixed with WT virus at a ratio of 9:1, 1:1 or 1:9, then applied to
492 HEL299 cells. After the virus was passaged three more times, Nanopore sequencing was performed on each
493 passage, to determine the percentage of viral genomes that contained the mutant or WT form of nsp15.

494

495 The mutant viruses are outcompeted by WT virus

496 To estimate the competitive fitness of the mutants vis-à-vis WT, we co-infected HEL299 cells with three
497 different WT:mutant ratios and then passaged the progeny virus three times; all this virus culturing was
498 done in the absence of compound. Each passage was submitted to Nanopore sequencing to assess
499 the percentage of mutant versus WT sequence in the virus population. This revealed that all nsp15
500 mutant forms of HCoV-229E were outcompeted by WT virus (Fig 3B). The two catalytic site mutants
501 ($G248V_{nsp15}$ and $H250Y_{nsp15}$) showed the highest fitness cost. Their virus populations almost exclusively
502 consisted of WT after four passages, even if the mutant was 9-fold in excess at the start of the
503 experiment. Also the $K60R_{nsp15}$ and particularly the $T66I_{nsp15}$ virus were readily overtaken by WT virus.
504 Hence, in line with their shifted growth curves in HEL299 cells (see above), the catalytic site mutant
505 viruses proved unable to compete with WT virus. The other two mutations, $K60R_{nsp15}$ and $T66I_{nsp15}$, had
506 less dramatic effect but still rendered the virus less fit in comparison to WT virus.

507

508 Elevated expression of interferon and related players in 509 innate immunity

510 So far, the only validated function of nsp15 is to avoid early induction of IFN-I by reducing the levels of
511 viral dsRNA replication intermediates [10-12]. Parallel to the viral growth experiments, we thus assessed
512 whether the mutants differed from WT virus in terms of induction of IFN-I and other innate immune
513 factors. The levels of bioactive IFN-α/β protein were determined in human macrophages, HEL299 and
514 16HBE cells, while all other factors were measured at transcript level and in HEL299 cells only. The data
515 are visualized as heatmaps in Fig 4, while the numeric data and levels of statistical significance are
516 provided in S3 Fig.

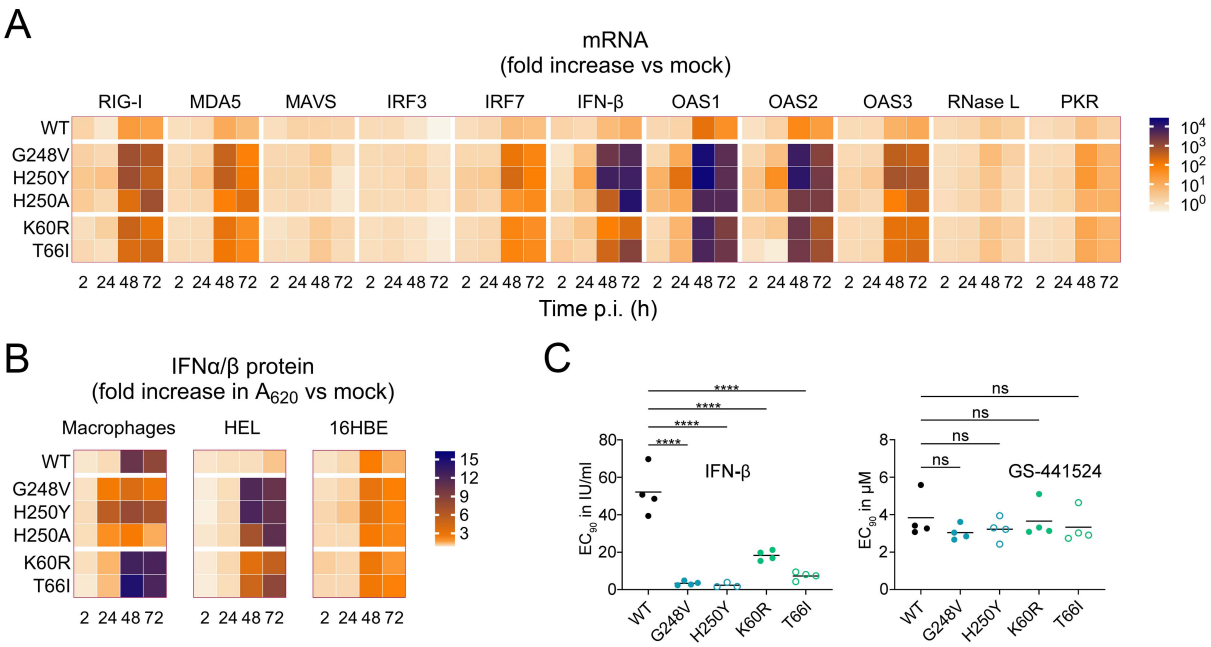

Fig 4. The nsp15-mutant HCoV-229E viruses boost the host cell's innate immune response. (A) mRNA levels (determined by RT-qPCR) for a range of innate immune factors, in HEL299 cells infected with WT or nsp15-mutant virus. (B) Levels of bioactive IFN-I in the supernatant of human macrophages, HEL299 cells or 16HBE cells infected with WT or mutant virus. For both heatmaps, detailed graphs containing the numeric values and statistical analysis are provided in S3 Fig. (C) The nsp15 mutations render HCoV-229E more sensitive to the antiviral effect of exogenous IFN-β, as determined by viral load assay in HEL299 cells. The graphs show the individual and mean values from four independent experiments. An ordinary one-way ANOVA with Dunnett's correction was used to analyze the differences in EC_{90}, comparing mutants to WT virus.

For WT virus (see top row in Fig 4B), the induction of IFN-I was evident at 48 and 72 h but not yet at 24 h p.i. The increases in bioactive IFN-I, compared to mock-infected cells, were up to 10-fold in macrophages, up to 2-fold in 16HBE cells and not seen (i.e. maximum 1.2-fold) in HEL299 cells (Fig 4B). The impact of the nsp15 mutations differed according to time and cell type and, overall, the viruses carrying EndoU catalytic site mutations had a different profile than the $K60R_{nsp15}$ and $T66I_{nsp15}$ mutants. When analyzed at 48 or 72 h p.i., macrophages infected with the $K60R_{nsp15}$ or $T66I_{nsp15}$ virus showed slightly higher levels of IFN-I than cells infected with WT virus. The $G248V_{nsp15}$, $H250Y_{nsp15}$ and $H250A_{nsp15}$ viruses not only showed the opposite profile (i.e. less IFN-I than WT at 48 and 72 h p.i.), but also differed from WT virus in showing an increase in IFN-I at 24 h p.i. Apparently, the levels of IFN-I induced by these mutant viruses within the first 24 h are sufficient to fully suppress their replication (as

537 evident from the growth curves above) which, in turn, prevents a further strong rise in IFN-I at later time
538 points. The early IFN-I induction was not seen in the other two cell types. In 16HBE cells analyzed at 48
539 h or 72 p.i., the nsp15 mutants showed modest increases in IFN-I versus WT, although the difference
540 reached significance ($P \leq 0.001$) for the $G248V_{nsp15}$ and $H250Y_{nsp15}$ viruses. In HEL cells, all nsp15
541 mutants generated markedly higher IFN-I levels than WT virus; the differences were more significant for
542 the three catalytic site mutants (9-fold; $P \leq 0.0001$ at 72 h p.i.) than for $K60R_{nsp15}$ (4-fold; ns) and $T66I_{nsp15}$
543 (7-fold, $P = 0.002$).

544 The panel of innate immune factors, determined at transcript level in HEL299 cells, consisted of (Fig
545 4A): the pathogen recognition receptors (PRRs) retinoic acid-inducible gene I (RIG-I) and melanoma
546 differentiation-associated protein 5 (MDA5); the signaling factors mitochondrial antiviral-signaling
547 protein (MAVS), interferon regulatory factor 3 (IRF3) and 7 (IRF7); IFN-β; and antiviral effectors 2′-5′-
548 oligoadenylate synthetases (OAS1-3), RNase L and protein kinase R (PKR). All nsp15 mutants
549 generated significantly higher mRNA levels than WT virus for RIG-I, MDA5, IRF7, OAS1-3 and PKR.
550 The increases were only evident at 48 and 72 h p.i., in line with the results obtained for the IFN-I bioassay
551 in HEL299 cells. Particularly abundant expression was seen for OAS-1 and OAS-2: at 48 h p.i., their
552 mRNA levels were 2000- to 25,000-fold increased versus mock, compared to 60- to 160-fold for WT
553 virus, giving high significance ($P \leq 0.001$) for each comparison between mutant and WT [see the numeric
554 values (log_{10} scale) and significance levels in S3 Fig). The catalytic site mutants showed higher
555 expression of the innate immune factors than the other two mutants. For instance, for the $G248V_{nsp15}$,
556 $H250Y_{nsp15}$ and $H250A_{nsp15}$ mutants, RIG-I mRNA was up to ~800-fold increased versus mock, while the
557 $K60R_{nsp15}$ and $T66I_{nsp15}$ mutants showed a maximum increase of ~300-fold. For MAVS and RNase L,
558 we observed no or only weak induction, regardless of whether the cells were infected with WT or mutant.
559 Finally, we observed that HCoV-229E infection slightly reduces the transcription of IRF3 (3-fold), and
560 that EndoU catalytic site mutations significantly ($P \leq 0.01$) revert this effect. This is in line with the finding
561 that PEDV EndoU was reported to degrade the mRNA of IRF3 [49]. We note, however, that our analysis
562 of innate immune factors looked only at their transcript levels, and not at their protein level, status of
563 activation (e.g. from phosphorylation) or downstream activity.

564

565

566 # The mutants are more sensitive to treatment with IFN-β

567 Considering that the EndoU-mutants induce higher levels of IFN-I effectors than WT virus, they may
568 also be more responsive to exogenous interferon. This was indeed demonstrated by Kindler et al. [11],
569 for H250A$_{nsp15}$-mutant HCoV-229E evaluated in human MRC5 cells. Hence, we determined the antiviral
570 activity of recombinant human IFN-β in HEL299 cells (Fig 4C), which are the same cell type as MRC5
571 (i.e. both are human fibroblast cells isolated from normal fetal lung tissue). RT-qPCR for viral load was
572 performed on the supernatants collected at day 3 p.i. Compared to WT virus, all nsp15-mutants exhibited
573 markedly lower EC_{90} values for IFN-β. The G248V$_{nsp15}$ and H250Y$_{nsp15}$ mutants showed a very strong
574 shift of ~20-fold. The T66I$_{nsp15}$ and K60R$_{nsp15}$ mutants were less affected (= ~7- and ~3-fold lower EC_{90}
575 value than WT, respectively), but still showed significantly ($P \leq 0.0001$) higher IFN-β sensitivity than WT.

576 Collectively, the following conclusions can be made from this phenotypic profiling of the nsp15-mutant
577 HCoV-229E viruses which arose under EPB-113 or 5h. Compared to WT virus, the mutants show an
578 altered IFN-I response, but the kinetics, intensity and consequences of this effect depend on the cell
579 type. Due to early induction of IFN-I, the EndoU catalytic site mutants are incapable of replicating in
580 macrophages. This aligns with two previous studies on EndoU-mutant forms of HCoV-229E and MHV
581 [10, 11]. In 16HBE cells, the mutants behave similarly to WT virus in terms of IFN-I induction and growth
582 kinetics. An intermediate profile is seen in HEL299 cells. Here, the nsp15 mutants are prominent
583 inducers of IFN-I and readily outcompeted by WT virus.

584

585 # EPB-113 combines a direct antiviral effect with a subtle
586 # boost in type I interferon

587 Considering that EPB-113 selects mutations in the EndoU catalytic core, we hypothesized that it might
588 act by altering the expression of IFN-I in CoV-infected cells. To test this hypothesis, we applied two
589 different variations to our antiviral assay. First, we determined the inhibitory activity of EPB-113 in
590 macrophages, HEL299 and 16HBE cells. Although EPB-113 proved nicely active in all three cell types,
591 the EC_{90} values were not identical. Compared to HEL299 cells, EPB-113 was 2-fold less potent in 16HBE
592 cells and 6-fold more potent in macrophages (Fig 5). We also observed a difference for GS-441524, in

593 line with a report that the metabolic activation of this nucleoside analogue is cell type-dependent [50].
594 For EPB-113, a parallel can be noticed with the findings in the previous section. Namely, the nsp15
595 disturbance by EPB-113 proved strongest in macrophages, in line with the prominent growth impairment
596 of EndoU-mutant viruses in this cell type. The activity of EPB-113 was slightly higher in HEL299 than in
597 16HBE cells, which agrees with the competitive growth defect of the nsp15-mutant viruses seen in the
598 former cell line. Still, EPB-113 exerted clear activity in 16HBE cells, in which the EndoU-mutant viruses
599 were hardly distinguishable from WT virus in terms of growth kinetics and IFN-I induction. This was a
600 first indication that the compound may have a second effect that does not involve the EndoU/IFN-I axis.

601

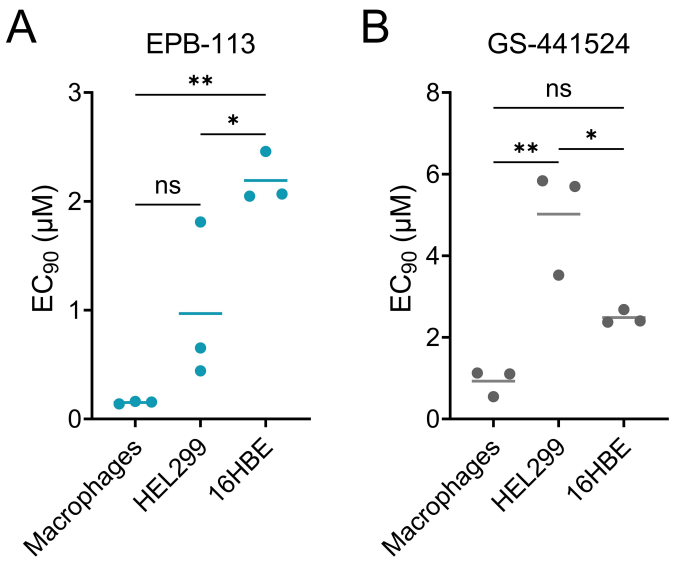

602

603 **Fig 5. The inhibitory potency of EPB-113 is cell-type dependent.** EC_{90} values of EPB-113 (A) and GS-441524
604 (B) for inhibition of HCoV-229E WT virus in human macrophages, HEL299 cells and 16HBE cells, based on viral
605 load assay. The graph shows the individual values and mean from three independent experiments. The differences
606 in EC_{90} values among the three cell lines were evaluated with a one-way ANOVA with Tukey multiple comparisons
607 post-hoc correction.

608

609 Secondly, we assessed whether EPB-113 changes the expression of IFN-β in HCoV-229E-infected
610 HEL299 cells. When the compound was added together with virus (= at 0 h p.i.), the levels of IFN-β
611 mRNA (assessed at 48 h p.i.) were similar in cells receiving no compound, EPB-113, GS-441524 or
612 nirmatrelvir (S4 Fig). Strikingly, when compound addition was postponed until 24 h p.i., which gave the

613 virus the chance to start replicating, we observed 48 h later a significant spike in IFN-β in the condition
614 receiving 1 μM of EPB-113 (Fig 6B). The spike was evident from both IFN-β mRNA quantification and
615 IFN-I bioassay. For this delayed treatment schedule, the dose-response curve showed an extra plateau
616 at exactly this concentration of EPB-113 (Fig 6A). The biphasic shape of the curve indicates a dual
617 antiviral mechanism, in which the compound's direct antiviral effect combines with an indirect effect
618 through boosting of IFN-I. While GS-441524 had no such effect when added at 24 h p.i., the M^{pro} inhibitor
619 nirmatrelvir effectuated a strong and dose-dependent increase in the levels of IFN-β mRNA and IFN-I
620 protein. The IFN-I increase in the presence of nirmatrelvir implies that, besides its role in polyprotein
621 cleavage, the M^{pro} of HCoV-229E has immune-evading activity, as already demonstrated for the M^{pro}
622 enzymes of MERS-CoV [51] and SARS-CoV-2 [52]. M^{pro} was shown to exhibit cleavage activity towards
623 different cellular proteins [53], including RIG-I [52] and other components of the innate immune response
624 [54]. For both EPB-113 and nirmatrelvir, delaying treatment until 24 h p.i. was essential to ensure the
625 accumulation of sufficient viral RNA to function as a pathogen-associated molecular pattern (PAMP).
626 Subsequently, inhibiting the immune evasion activities of either nsp15 or M^{Pro} led to a significant increase
627 in interferon levels in response to the pre-existing viral RNA.

628

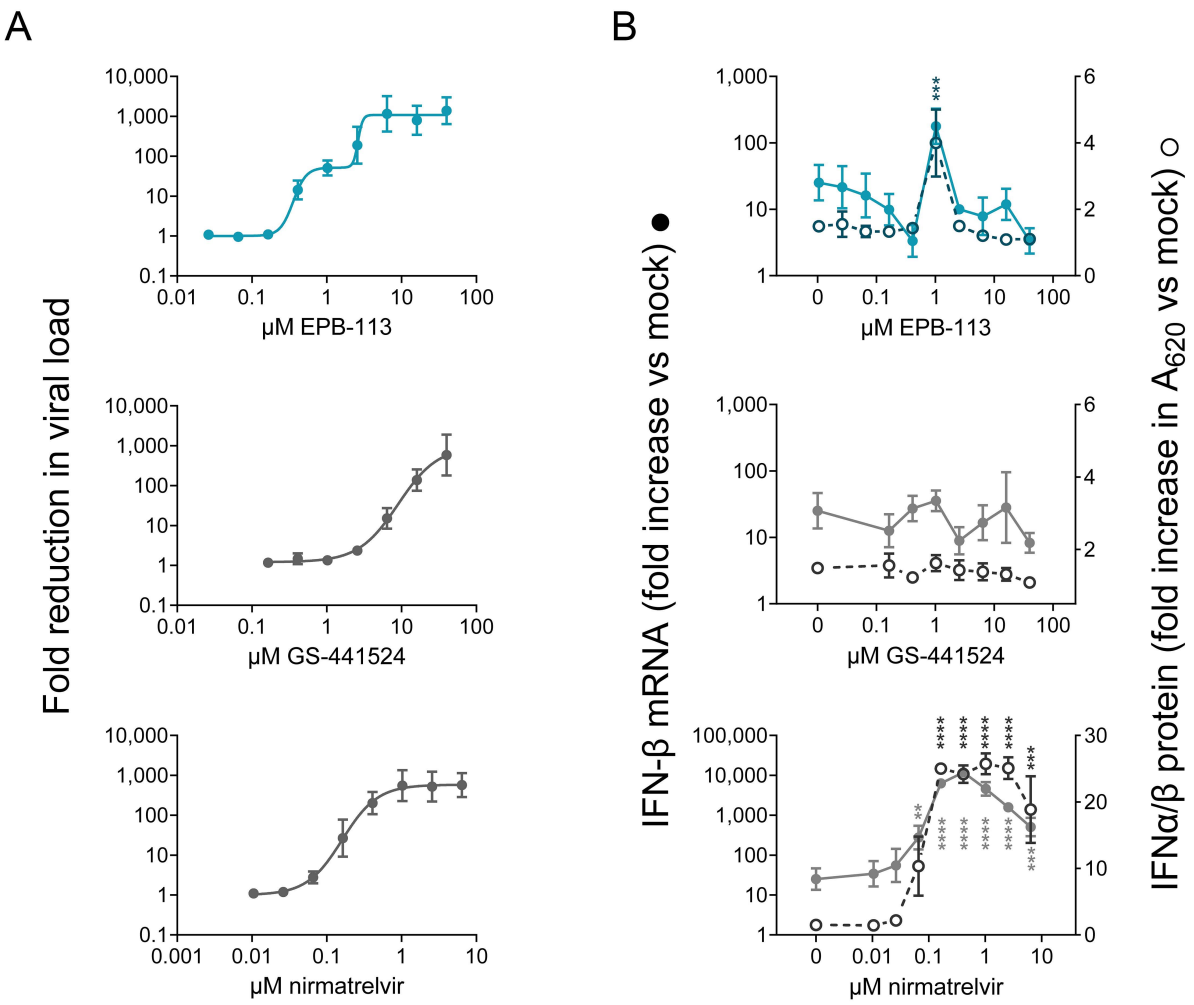

Fig 6. The anti-HCoV-229E activity of EPB-113 involves induction of IFN-I. Compound addition to HEL299 cells infected with HCoV-229E WT was delayed until 24 h p.i. and 48 h later, samples were collected for assessment of (A) viral load and (B) levels of IFN-I (left Y-axis: IFN-β mRNA; right Y-axis: bioactive IFN-I). GS-441524 and nirmatrelvir were included as reference compounds. Data points are the mean ± SEM (N=4). Statistical analysis was performed using a one-way ANOVA with Dunnett's correction for multiple comparisons, to compare each compound concentration to untreated virus control (0 μM).

639 # EPB-113 also acts at a post-entry and intermediate stage in
640 first-cycle HCoV-229E replication

641 Since the above findings provided strong support for a direct effect of EPB-113 on viral replication, we
642 wanted to gain basic insight into which stage of the replication cycle could be affected. To address this,
643 we conducted one-cycle time-of-addition experiments in HCoV-229E-infected HEL299 cells. Besides
644 EPB-113, we included four reference compounds: E64d (an inhibitor of cathepsin-mediated entry of the
645 HCoV-229E ATCC strain) [55]; nirmatrelvir (an M^{pro} inhibitor); GS-441524 (an RdRp inhibitor that
646 terminates viral RNA synthesis); and K22 (which prevents nsp6-mediated formation of the double-
647 membrane vesicle structures where viral RNA synthesis takes place) [56]. The compounds were added
648 to the cells at either 30 min before or several time points after virus infection. At 16 h p.i. (previously
649 determined to mark the end of one HCoV-229E replication cycle), the cells were collected to quantify
650 the level of intracellular viral RNA by RT-qPCR. We also analyzed a condition at 2 h p.i. (= RNA from
651 input virus) to express the data as the fold increase in viral RNA at 16 h p.i. versus input. In the absence
652 of compound, this fold increase was ~10,000-fold (= factor of 4 $\log_{10}$ in Fig 7).

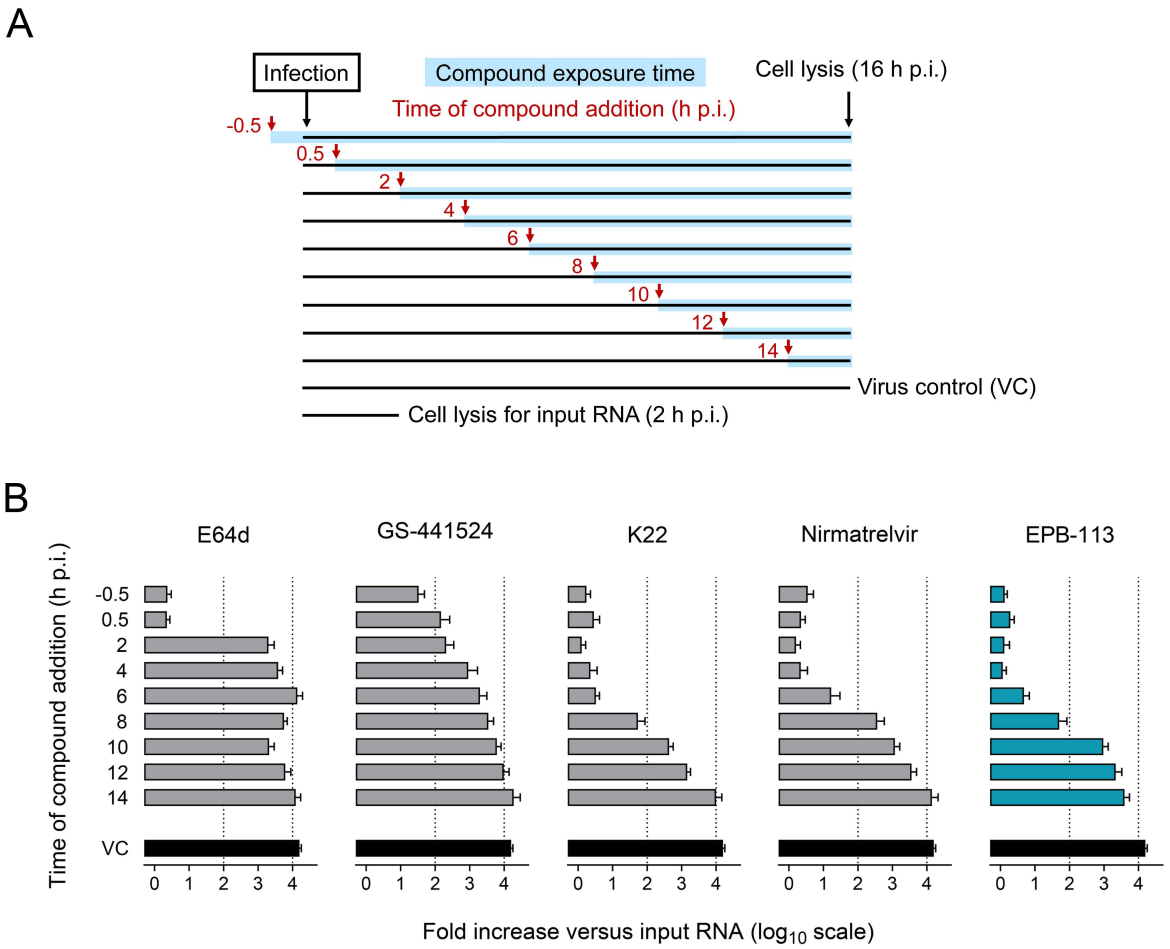

Fig 7. Action point of EPB-113 and reference compounds in a one-cycle time-of-addition assay. (A) Experimental setup. (B) Timewise, EPB-113 has a similar action point as K22, located at an intermediate stage in HCoV-229E replication. The fold increase in intracellular viral RNA is expressed relative to the amount of input RNA at 2 h p.i. Compound concentrations: 15 μM E64d; 15 μM GS-441524; 15 μM K22 [56]; 3 μM nirmatrelvir; and 15 μM EPB-113. Data points are the mean ± SEM (N=3).

Whereas the entry inhibitor E64d lost all of its activity when added at 2 or more hours p.i., EPB-113 and K22 still had profound effect on the level of viral RNA (= ~300 times less than in the virus control) when added at 8 h p.i. (Fig 7). Nirmatrelvir already started to lose activity at 8 h p.i. (only 40-fold reduction versus virus control), consistent with inhibition of protease activity. GS-441524 was already less active when added at 4 h p.i., indicating that this nucleoside analogue requires a few hours to attain a sufficient level of its active 5′-triphosphate metabolite in HEL299 cells. The experiment further showed that neither of the tested compounds, including EPB-113, act at the stages of virus maturation or budding. Inhibitors of the latter processes would show no inhibition in our assay, since we measured the viral RNA levels

668 inside the cells and not the progeny virus released in the supernatant. Besides, the data corroborate
669 that EPB-113 also interferes with viral replication in a direct manner that does not involve IFN-I. The
670 mRNA for IFN-I became only detectable at 48 h p.i. of HEL299 cells (see above). Since the level of viral
671 RNA, produced within one replication cycle of ~16 h, is too low to induce a measurable level of IFN-I,
672 the strong activity of EPB-113 in the time-of-addition assay must be independent of this cytokine.

673 Taken together, the above results demonstrate that EPB-113 exhibits a dual effect on HCoV-229E
674 replication. The first effect is IFN-independent and evident from the nice activity in 16HBE cells and
675 strong suppression of first-cycle viral RNA synthesis. The second and indirect effect of EPB-113 occurs
676 via subtle boosting of IFN-I by disturbing EndoU activity. This effect provides an explanation for the
677 compound's superior activity in macrophages and biphasic dose-response curve in HEL299 cells.

678

679 The binding of EPB-113 to nsp15 destabilizes the protein 680 and stimulates its EndoU activity

681 In the final part, we used different biophysical and biochemical methods to study the potential binding
682 interaction between nsp15 protein and EPB-113, and how this binding could change the EndoU activity
683 of nsp15. The nsp15 proteins of HCoV-229E and SARS-CoV-2 were expressed in *E. coli* as described
684 by others [7, 32] and the hexameric proteins were purified by size-exclusion chromatography.
685 Additionally, dynamic light scattering (DLS) analysis confirmed that the two proteins were ≥98%
686 hexameric (S1 Fig).

687 Using a thermal shift assay, we found that EPB-113 causes quite pronounced reduction in the
688 thermostability of nsp15, producing a shift in the melting temperature (T_m) of 4°C (Fig 8A). The shift was
689 comparable for the proteins of HCoV-229E and SARS-CoV-2. It required a fairly high concentration of
690 100 μM EPB-113, which represents a 17-fold molar excess compared to the concentration of 6 μM for
691 nsp15 protein. The thermal shift was not at all observed with amine EPB-102, the analogue lacking the
692 guanidine function that exhibited much weaker anti-HCoV-229E activity in HEL299 cells (15-fold higher
693 EC_{50}, see first part of the results). The binding of EPB-113 to nsp15 was confirmed by surface plasmon
694 resonance, in which we immobilized nsp15 to the chip as ligand, then used EPB-113 and EPB-102 as
695 analytes. The sensorgrams (Fig 8B) show dose-dependent binding of EPB-113 to nsp15, with a similar

profile for the HCoV-229E and SARS-CoV-2 proteins. The binding was markedly less with EPB-102 (5- to 8-fold less RU at 100 μM).

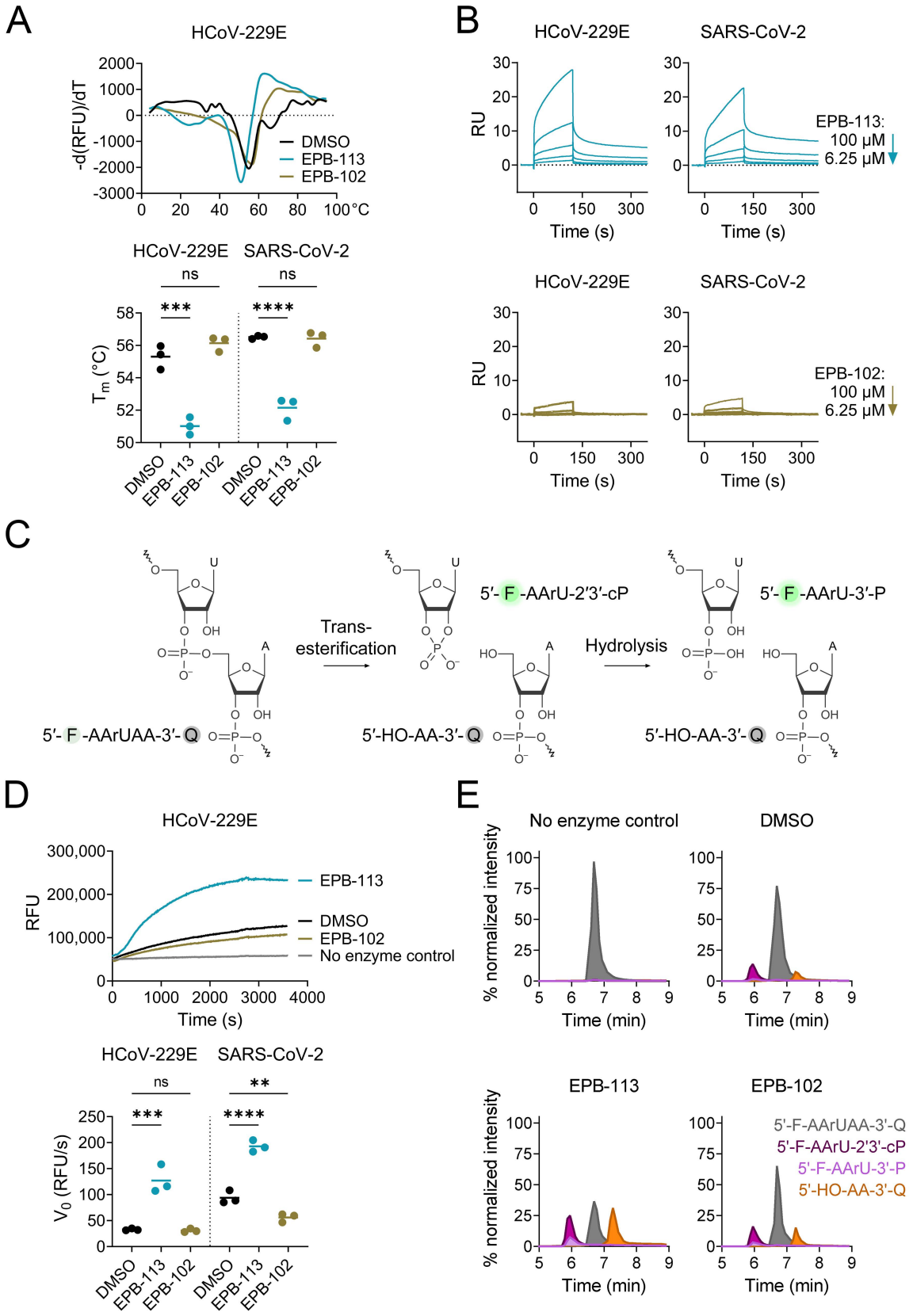

699 **Fig 8. EPB-113 binds to hexameric nsp15 protein and enhances the EndoU cleavage reaction.** (A) Thermal
700 shift assay showing the decrease in T_m when 6 μM of nsp15 protein was incubated with 100 μM EPB-113. The
701 controls contained 100 μM EPB-102 or the equivalent amount (= 5%) of DMSO. The top panel shows the curve of
702 one representative experiment. The graph (bottom panel) shows the melting temperatures (individual and mean
703 values) in three independent experiments. Statistical significance was determined with an ordinary one-way ANOVA
704 with Dunnett's correction. (B) Dose-dependent binding between EPB-113 (top panels) or EPB-102 (bottom panels)
705 and recombinant nsp15 from HCoV-229E (left panels) or SARS-CoV-2 (right panels), assessed by surface-plasmon
706 resonance. RU: resonance units. (C) Scheme of the two-step EndoU cleavage reaction. (D) FRET assay in the
707 presence of 100 μM EPB-113, 100 μM EPB-102 or the equivalent amount (= 5%) of DMSO. RFU: relative
708 fluorescence units. An example of the real-time fluorescence curves is shown in the top panel, while the graph in
709 the bottom panel shows the initial reaction velocity (V_0) derived from the 5-10 min interval. Individual and mean data
710 from N=3. (E) HPLC-MS analysis on samples collected after 1 h reaction time. In the chromatograms, the colors
711 indicate the FRET substrate; 2′,3′-cyclic intermediate; 5′-hydroxylated product; and 3′-phosphorylated product. The
712 Y-axis shows the % normalized intensity.

713

714 To next investigate the impact of EPB-113 on EndoU cleavage, we conducted a convenient fluorescence
715 resonance energy transfer (FRET) assay that allows to follow the reaction (Fig 8C) in real-time. Quite
716 intriguingly, EPB-113 was found to enhance the EndoU cleavage reaction (Fig 8D). At 100 μM EPB-113,
717 the initial reaction velocity (V_0) was increased by about 2- (SARS-CoV-2) or 4-fold (HCoV-229E)
718 compared to the DMSO control condition ($P < 0.0001$). Also this effect was not observed with EPB-102.
719 The activating effect of EPB-113 was also evident when we conducted HPLC-MS analysis on the
720 mixtures after 1 h reaction time. This method enabled to discriminate between the starting substrate; 5′-
721 hydroxylated reaction product; 2′,3′-cyclic phosphate reaction intermediate; and 3′-phosphorylated
722 reaction product (see reaction scheme in Fig 8C). The latter two cannot be distinguished in the FRET
723 assay, since they both carry the fluorophore. Although care should be taken when interpreting HPLC-
724 MS peak areas in a quantitative manner, the chromatograms (Fig 8E) show that, in the DMSO control
725 and EPB-102 samples, the 5′-hydroxylated product and 2′,3′-cyclic phosphate intermediate attained only
726 low levels after 1 h reaction time. The minute amount of the 3′-phosphorylated product confirms a
727 previous report that the 2′,3′-cyclic intermediate undergoes slow hydrolysis to this 3′-end product [32].
728 In the EPB-113 sample, both 5′- and 3′-end products as well as the 2′,3′-cyclic intermediate showed
729 markedly higher peak areas, confirming that the compound stimulates the reaction. Together, these data

730 corroborate that EPB-113 induces prominent activation of the cleavage reaction, while not affecting the

731 relative abundance of the cyclic intermediate and final 3′-phosphate product.

732 # Discussion

733 In this study, a detailed mechanistic investigation on the CoV replication inhibitor EPB-113 led to the
734 discovery of a novel antiviral concept targeting the viral nsp15 protein. Additionally, our research
735 highlights the broader importance of nsp15 for viral replication, extending beyond its EndoU activity and
736 its role in evading innate immunity.

737 Our findings challenge the conventional pharmacological view that disrupting the function of nsp15 in
738 virus-infected cells is best accomplished through inhibition of the EndoU-mediated RNA cleavage
739 reaction. Based on this concept, the search for nsp15 inhibitors has typically relied on an enzymatic
740 FRET assay that is suitable for high-throughput screening. Several hit compounds identified with the
741 nsp15 protein from SARS-CoV [25] or SARS-CoV-2 [26-30] demonstrated favorable IC_{50} values in a
742 FRET or similar enzymatic EndoU assay. However, in all cases, the compounds showed disappointing
743 inhibitory activity in CoV-infected cells. Since these compounds have diverse chemical structures, it is
744 unlikely that poor cell permeability is the sole issue. Rather, it may be that, unless a compound achieves
745 complete inhibition of EndoU cleavage, viral replication cannot be effectively suppressed. Alternatively,
746 the issue may be methodological: enzymatic EndoU assays may not accurately capture the complex
747 functions of nsp15 in viral replication, while antiviral assays in interferon-deficient cell lines, such as Vero
748 cells, overlook potential IFN induction by an EndoU inhibitor [38].

749 Our study with EPB-113 introduces a third and previously unrecognized possibility: disrupting the
750 functions of nsp15 in virus-infected cells may be better achieved with an nsp15 binder that alters the
751 protein's conformation in a way that enhances EndoU cleavage. The concept of enzyme activation offers
752 several advantages, including the potential to achieve strong efficacy within cells, even if the drug only
753 moderately activates the enzyme [57]. Although the activation by EPB-113 may seem modest based on
754 fluorographs from the FRET assay, this effect was confirmed by HPLC-MS analysis which showed
755 pronounced increase of the 5′-hydroxylated product, the 3′-phosphorylated product and the 2′-3′-cyclic
756 intermediate. EPB-113 could induce these effects by causing a conformational change in the nsp15
757 hexameric structure, as suggested by the thermal shift assay. The reduction of T_m caused by EPB-113
758 is significant and contrasts with the effect reported for tipiracil [31], a UMP analogue that causes modest
759 inhibition of the EndoU reaction and a slight increase (0.5 °C) in the thermostability of SARS-CoV-2

760 nsp15. In cryo-EM studies, nsp15 apoprotein is described as a highly flexible protein with 'wobbling'
761 EndoU domains that are stabilized upon RNA binding [32]. Although the specific structural changes
762 induced by EPB-113 remain speculative, we hypothesize that the compound might alter conformational
763 flexibility, inducing an RNA-bound state that is catalytically favorable, similar to the mechanism proposed
764 for the EndoU-stimulating effect of Mn^{2+} [58, 59]. Since the positively charged guanidine function (which
765 is fully protonated at physiological pH) is necessary for both the EndoU stimulation and strong antiviral
766 activity, EPB-113 may enhance the interaction between the RNA ligand and the negatively charged
767 surface of EndoU [33]. The idea that EPB-113 acts as a catalytic activator of EndoU aligns with its
768 resistance profile, as the virus escaped the compound by losing this enzymatic activity. A recent analysis
769 of the physiologic substrates of MHV EndoU suggested that its cleavage of specific motifs in viral
770 positive-sense RNA occurs in a regulated manner, to partially inhibit negative-strand RNA synthesis and
771 prevent accumulation of viral dsRNA [9]. It is possible that EPB-113 disrupts this finely balanced EndoU
772 activity. In summary, harnessing nsp15 for antiviral purposes may require rethinking the pharmacological
773 mechanisms best suited to achieve this objective.

774 As the first molecule reported to strongly suppress CoV replication in cells by binding to nsp15, EPB-
775 113 represents a unique tool for unravelling the functions of nsp15 beyond its role as an EndoU. An *in*
776 *silico* analysis, pending experimental validation, predicted a crucial role for nsp15 as the central scaffold
777 of the RTC structure [60]. Given that EPB-113 potently suppresses the replication of HCoV-229E in
778 16HBE cells, where the virus does not require a functional EndoU for replication, it is plausible that the
779 compound disrupts a structural function of nsp15. However, in HEL299 cells, EPB-113 exerts a second,
780 EndoU-dependent effect. The dual mechanism is evident from the biphasic dose-response curve and
781 subtle increase in IFN-I observed when the compound was added at 24 h post-infection. At high
782 concentrations, the direct effect of EPB-113 on nsp15 is dominant, whereas at intermediate
783 concentrations (~1 μM), the induced IFN-I helps to halt viral replication. The compound's direct effect is
784 further demonstrated by its strong activity in the one-cycle time-of-addition assay. Overall, the inhibitory
785 profile of EPB-113 strongly supports the idea that nsp15 combines roles in immune evasion and RNA
786 synthesis regulation.

787 Our phenotypic profiling of EndoU-mutant viruses confirms that, at least for HCoV-229E, having a
788 functional EndoU offers a clear advantage to the virus. At first sight, this seems contradictory to reports
789 of efficient replication of EndoU-deficient CoVs in various cell models [23, 61]. However, these studies

790 typically use immortalized cell lines, many of which have defects in the IFN-I pathway. Consistent with
791 a previous study [11], we confirm that EndoU-deficient HCoV-229E viruses (bearing nsp15 mutations
792 G248V, H250Y or H250A) trigger an early IFN-I response in human macrophages, rendering them
793 unable to replicate in these cells. While the mutants replicate efficiently in human lung fibroblasts, virus
794 competition experiments reveal that they are easily outcompeted by WT virus. The vulnerability of the
795 mutants stems from their ability to excessively stimulate the innate immune response, activating several
796 layers of defense, including IFN-I, PRRs, signaling factors and antiviral effectors. These responses
797 make the mutants more sensitive to IFN-I, amplifying their elimination when WT virus is also present.

798 Compared to HCoV-229E, SARS-CoV-2 may be even more dependent on EndoU for replication.
799 Mutations $G248V_{nsp15}$, $H250Y_{nsp15}$ and $H250A_{nsp15}$, which are viable for HCoV-229E, are not tolerated in
800 SARS-CoV-2. However, we successfully rescued two reverse-engineered SARS-CoV-2 mutants with
801 substitution $K61R_{nsp15}$ or $V67I_{nsp15}$ adjacent to the catalytic site. Using these mutants, we confirmed that
802 nsp15 is also the target for EPB-113 in SARS-CoV-2. Future development of EPB-113 will require
803 structural optimization, to achieve sufficient anti-SARS-CoV-2 activity.

804 Evidence suggests that the immune-evading function of nsp15 may not solely depend on EndoU
805 cleavage of specific motifs in viral RNA [9, 12], but could also involve cytoprotective effects or
806 interactions between nsp15 and a cellular protein involved in IFN production or cell cycle regulation [13,
807 14, 17]. While some of these functions have been proposed based on nsp15 transfection studies, they
808 await confirmation in authentic virus models. We cannot rule out the possibility that EPB-113 acts on
809 one of these alternative nsp15 functions. Considering recent links between nsp15 and stress granules
810 [18-20], one might hypothesize that EPB-113 induces a state of cell stress. However, this is highly
811 unlikely, as the compound has low cytotoxicity, even at concentrations that are well above its antiviral
812 range.

813 In conclusion, while the many unknowns regarding the function of nsp15 in CoV replication present a
814 challenge for antiviral drug development, our study demonstrates that nsp15 is a valid target for inhibiting
815 CoV replication. We provide evidence that strong antiviral activity can be achieved with a compound,
816 like EPB-113, which alters the conformation of nsp15 and enhances its EndoU activity. This mechanism
817 disrupts viral RNA synthesis while subtly boosting IFN-I production, offering a unique combination of

818 direct antiviral and indirect immunomodulatory effects that make the concept of nsp15 binders highly
819 attractive for antiviral therapy.

Acknowledgements

We wish to thank L. Delarbre, B. Ramos, E. Bernaerts and S. Wouters for excellent technical assistance and V. Thiel, B. Canard, P. Hoet, P. J. Bredenbeek, D. Jochmans, X. Saelens and P.-Y. Shi for the kind gift of viruses, plasmids or cells. Images were produced using Graphpad Prism 10.3.1 (GraphPad Software, Boston, Massachusetts USA), the UCSF Chimera package [62] from the Resource for Biocomputing, Visualization, and Informatics at the University of California, San Francisco (supported by NIH P41-GM103311); ESPript [63], SynergyFinder+ [48] and Marvin (https://www.chemaxon.com).

828 # References

829 1. World Health Organization. WHO COVID-19 Dashboard. [23/08/2024]. Available from:
830 https://data.who.int/dashboards/covid19/cases.
831 2. Infectious Diseases Society of America. IDSA guidelines on the treatment and management of patients
832 with COVID-19. [23/08/2024]. Available from: https://www.idsociety.org/COVID19guidelines.
833 3. V'Kovski P, Kratzel A, Steiner S, Stalder H, Thiel V. Coronavirus biology and replication: implications for
834 SARS-CoV-2. Nat Rev Microbiol. 2021;19(3):155-70. Epub 2020/10/30. doi: 10.1038/s41579-020-00468-6.
835 PubMed PMID: 33116300; PubMed Central PMCID: PMCPMC7592455.
836 4. Lou Z, Rao Z. The life of SARS-CoV-2 inside cells: replication-transcription complex assembly and
837 function. Annu Rev Biochem. 2022;91:381-401. doi: 10.1146/annurev-biochem-052521-115653. PubMed PMID:
838 35729072.
839 5. Li G, Hilgenfeld R, Whitley R, De Clercq E. Therapeutic strategies for COVID-19: progress and lessons
840 learned. Nat Rev Drug Discov. 2023;22(6):449-75. Epub 20230419. doi: 10.1038/s41573-023-00672-y. PubMed
841 PMID: 37076602; PubMed Central PMCID: PMCPMC10113999.
842 6. Minkoff JM, tenOever B. Innate immune evasion strategies of SARS-CoV-2. Nat Rev Microbiol.
843 2023;21(3):178-94. Epub 20230111. doi: 10.1038/s41579-022-00839-1. PubMed PMID: 36631691; PubMed
844 Central PMCID: PMCPMC9838430.
845 7. Ivanov KA, Hertzig T, Rozanov M, Bayer S, Thiel V, Gorbalenya AE, et al. Major genetic marker of
846 nidoviruses encodes a replicative endoribonuclease. Proc Natl Acad Sci U S A. 2004;101(34):12694-9. Epub
847 2004/08/12. doi: 10.1073/pnas.0403127101. PubMed PMID: 15304651; PubMed Central PMCID:
848 PMCPMC514660.
849 8. Deng X, Baker SC. An "old" protein with a new story: coronavirus endoribonuclease is important for
850 evading host antiviral defenses. Virology. 2018;517:157-63. Epub 2018/01/09. doi: 10.1016/j.virol.2017.12.024.
851 PubMed PMID: 29307596; PubMed Central PMCID: PMCPMC5869138.
852 9. Ancar R, Li Y, Kindler E, Cooper DA, Ransom M, Thiel V, et al. Physiologic RNA targets and refined
853 sequence specificity of coronavirus EndoU. RNA. 2020;26(12):1976-99. Epub 2020/09/30. doi:
854 10.1261/rna.076604.120. PubMed PMID: 32989044; PubMed Central PMCID: PMCPMC7668261.
855 10. Deng X, Hackbart M, Mettelman RC, O'Brien A, Mielech AM, Yi G, et al. Coronavirus nonstructural protein
856 15 mediates evasion of dsRNA sensors and limits apoptosis in macrophages. Proc Natl Acad Sci U S A.
857 2017;114(21):E4251-E60. doi: 10.1073/pnas.1618310114. PubMed PMID: 28484023.
858 11. Kindler E, Gil-Cruz C, Spanier J, Li Y, Wilhelm J, Rabouw HH, et al. Early endonuclease-mediated evasion
859 of RNA sensing ensures efficient coronavirus replication. PLoS Pathog. 2017;13(2):e1006195. Epub 2017/02/06.
860 doi: 10.1371/journal.ppat.1006195. PubMed PMID: 28158275; PubMed Central PMCID: PMCPMC5310923.

861 12. Hackbart M, Deng X, Baker SC. Coronavirus endoribonuclease targets viral polyuridine sequences to
862 evade activating host sensors. Proc Natl Acad Sci USA. 2020;117(14):8094-103. Epub 2020/03/22. doi:
863 10.1073/pnas.1921485117. PubMed PMID: 32198201; PubMed Central PMCID: PMCPMC7149396.
864 13. Gordon DE, Jang GM, Bouhaddou M, Xu J, Obernier K, White KM, et al. A SARS-CoV-2 protein interaction
865 map reveals targets for drug repurposing. Nature. 2020;583(7816):459-68. Epub 2020/05/01. doi: 10.1038/s41586-
866 020-2286-9. PubMed PMID: 32353859; PubMed Central PMCID: PMCPMC7431030.
867 14. Zhang D, Ji L, Chen X, He Y, Sun Y, Ji L, et al. SARS-CoV-2 Nsp15 suppresses type I interferon production
868 by inhibiting IRF3 phosphorylation and nuclear translocation. iScience. 2023;26(9):107705. Epub 20230823. doi:
869 10.1016/j.isci.2023.107705. PubMed PMID: 37680466; PubMed Central PMCID: PMCPMC10480782.
870 15. Lei Y, Moore CB, Liesman RM, O'Connor BP, Bergstralh DT, Chen ZJ, et al. MAVS-mediated apoptosis
871 and its inhibition by viral proteins. PLoS One. 2009;4(5):e5466. Epub 2009/05/01. doi:
872 10.1371/journal.pone.0005466. PubMed PMID: 19404494; PubMed Central PMCID: PMCPMC2674933.
873 16. Hayn M, Hirschenberger M, Koepke L, Nchioua R, Straub JH, Klute S, et al. Systematic functional analysis
874 of SARS-CoV-2 proteins uncovers viral innate immune antagonists and remaining vulnerabilities. Cell Rep.
875 2021:109126. Epub 2021/05/12. doi: 10.1016/j.celrep.2021.109126. PubMed PMID: 33974846; PubMed Central
876 PMCID: PMCPMC8078906.
877 17. Bhardwaj K, Liu P, Leibowitz JL, Kao CC. The coronavirus endoribonuclease nsp15 interacts with
878 retinoblastoma tumor suppressor protein. J Virol. 2012;86(8):4294-304. Epub 2012/02/04. doi: 10.1128/JVI.07012-
879 11. PubMed PMID: 22301153; PubMed Central PMCID: PMCPMC3318636.
880 18. Gao B, Gong X, Fang S, Weng W, Wang H, Chu H, et al. Inhibition of anti-viral stress granule formation by
881 coronavirus endoribonuclease nsp15 ensures efficient virus replication. PLoS Pathog. 2021;17(2):e1008690. Epub
882 2021/02/27. doi: 10.1371/journal.ppat.1008690. PubMed PMID: 33635931; PubMed Central PMCID:
883 PMCPMC7946191.
884 19. Zhao J, Feng D, Zhao Y, Huang M, Zhang X, Zhang G. Role of stress granules in suppressing viral
885 replication by the infectious bronchitis virus endoribonuclease. J Virol. 2022;96(12):e0068622. Epub 20220531. doi:
886 10.1128/jvi.00686-22. PubMed PMID: 35638780; PubMed Central PMCID: PMCPMC9215229.
887 20. Dolliver SM, Kleer M, Bui-Marinos MP, Ying S, Corcoran JA, Khaperskyy DA. Nsp1 proteins of human
888 coronaviruses HCoV-OC43 and SARS-CoV2 inhibit stress granule formation. PLoS Pathog. 2022;18(12):e1011041.
889 Epub 20221219. doi: 10.1371/journal.ppat.1011041. PubMed PMID: 36534661; PubMed Central PMCID:
890 PMCPMC9810206.
891 21. Deng X, van Geelen A, Buckley AC, O'Brien A, Pillatzki A, Lager KM, et al. Coronavirus endoribonuclease
892 activity in porcine epidemic diarrhea virus suppresses type I and type III interferon responses. J Virol.
893 2019;93(8):e02000-18. Epub 2019/02/08. doi: 10.1128/JVI.02000-18. PubMed PMID: 30728254; PubMed Central
894 PMCID: PMCPMC6450110.

895 22. Comar CE, Otter CJ, Pfannenstiel J, Doerger E, Renner DM, Tan LH, et al. MERS-CoV endoribonuclease
896 and accessory proteins jointly evade host innate immunity during infection of lung and nasal epithelial cells. Proc
897 Natl Acad Sci U S A. 2022;119(21):e2123208119. Epub 20220520. doi: 10.1073/pnas.2123208119. PubMed PMID:
898 35594398; PubMed Central PMCID: PMCPMC9173776.
899 23. Otter CJ, Bracci N, Parenti NA, Ye C, Asthana A, Blomqvist EK, et al. SARS-CoV-2 nsp15
900 endoribonuclease antagonizes dsRNA-induced antiviral signaling. Proc Natl Acad Sci U S A.
901 2024;121(15):e2320194121. Epub 20240403. doi: 10.1073/pnas.2320194121. PubMed PMID: 38568967; PubMed
902 Central PMCID: PMCPMC11009620.
903 24. Xie Y, Chen C, Zhang D, Jiao Z, Chen Y, Wang G, et al. Diversity for endoribonuclease nsp15-mediated
904 regulation of alpha-coronavirus propagation and virulence. Microbiol Spectr. 2023;11(6):e0220923. Epub 20231108.
905 doi: 10.1128/spectrum.02209-23. PubMed PMID: 37938022; PubMed Central PMCID: PMCPMC10715224.
906 25. Ortiz-Alcantara JM, Bhardwaj K, Palaninathan S, Frieman M, Baric RS, Kao CC. Small molecule inhibitors
907 of the SARS-CoV nsp15 endoribonuclease. Virus Adapt Treat. 2010;2:125-33. doi: 10.2147/vaat.s12733.
908 26. Canal B, Fujisawa R, McClure AW, Deegan TD, Wu M, Ulferts R, et al. Identifying SARS-CoV-2 antiviral
909 compounds by screening for small molecule inhibitors of nsp15 endoribonuclease. Biochem J. 2021;478(13):2465-
910 79. Epub 2021/07/02. doi: 10.1042/BCJ20210199. PubMed PMID: 34198324.
911 27. Choi R, Zhou M, Shek R, Wilson JW, Tillery L, Craig JK, et al. High-throughput screening of the ReFRAME,
912 Pandemic Box, and COVID Box drug repurposing libraries against SARS-CoV-2 nsp15 endoribonuclease to identify
913 small-molecule inhibitors of viral activity. PLoS One. 2021;16(4):e0250019. Epub 2021/04/23. doi:
914 10.1371/journal.pone.0250019. PubMed PMID: 33886614; PubMed Central PMCID: PMCPMC8062000.
915 28. Hong S, Seo SH, Woo SJ, Kwon Y, Song M, Ha NC. Epigallocatechin gallate inhibits the uridylate-specific
916 endoribonuclease nsp15 and efficiently neutralizes the SARS-CoV-2 strain. J Agric Food Chem. 2021;69(21):5948-
917 54. Epub 2021/05/22. doi: 10.1021/acs.jafc.1c02050. PubMed PMID: 34015930; PubMed Central PMCID:
918 PMCPMC8146138.
919 29. Chen J, Farraj RA, Limonta D, Tabatabaei Dakhili SA, Kerek EM, Bhattacharya A, et al. Reversible and
920 irreversible inhibitors of coronavirus Nsp15 endoribonuclease. J Biol Chem. 2023;299(11):105341. Epub 20231011.
921 doi: 10.1016/j.jbc.2023.105341. PubMed PMID: 37832873; PubMed Central PMCID: PMCPMC10656235.
922 30. Ma Y, Luo M, Deng Y, Yang X, Wang X, Chen G, et al. Antibiotic-induced primary biles inhibit SARS-CoV-
923 2 endoribonuclease nsp15 activity in mouse gut. Front Cell Infect Microbiol. 2022;12:896504. Epub 2022/08/16.
924 doi: 10.3389/fcimb.2022.896504. PubMed PMID: 35967852; PubMed Central PMCID: PMCPMC9366059.
925 31. Kim Y, Wower J, Maltseva N, Chang C, Jedrzejczak R, Wilamowski M, et al. Tipiracil binds to uridine site
926 and inhibits nsp15 endoribonuclease NendoU from SARS-CoV-2. Commun Biol. 2021;4(1):193. Epub 2021/02/11.
927 doi: 10.1038/s42003-021-01735-9. PubMed PMID: 33564093.

928 32. Pillon MC, Frazier MN, Dillard LB, Williams JG, Kocaman S, Krahn JM, et al. Cryo-EM structures of the
929 SARS-CoV-2 endoribonuclease nsp15 reveal insight into nuclease specificity and dynamics. Nat Commun.
930 2021;12(1):636. Epub 2021/01/29. doi: 10.1038/s41467-020-20608-z. PubMed PMID: 33504779; PubMed Central
931 PMCID: PMCPMC7840905.
932 33. Frazier MN, Dillard LB, Krahn JM, Perera L, Williams JG, Wilson IM, et al. Characterization of SARS2
933 nsp15 nuclease activity reveals it's mad about U. Nucleic Acids Res. 2021;49(17):10136-49. Epub 2021/08/18. doi:
934 10.1093/nar/gkab719. PubMed PMID: 34403466; PubMed Central PMCID: PMCPMC8385992.
935 34. Frazier MN, Wilson IM, Krahn JM, Butay KJ, Dillard LB, Borgnia MJ, et al. Flipped over U: structural basis
936 for dsRNA cleavage by the SARS-CoV-2 endoribonuclease. Nucleic Acids Res. 2022;50(14):8290-301. Epub
937 2022/07/09. doi: 10.1093/nar/gkac589. PubMed PMID: 35801916; PubMed Central PMCID: PMCPMC9371922.
938 35. Ito F, Yang H, Zhou ZH, Chen XS. Structural basis for polyuridine tract recognition by SARS-CoV-2 Nsp15.
939 Protein Cell. 2024;15(7):547-52. Epub 20240413. doi: 10.1093/procel/pwae009. PubMed PMID: 38613382;
940 PubMed Central PMCID: PMCPMC11214832.
941 36. Ricagno S, Egloff MP, Ulferts R, Coutard B, Nurizzo D, Campanacci V, et al. Crystal structure and
942 mechanistic determinants of SARS coronavirus nonstructural protein 15 define an endoribonuclease family. Proc
943 Natl Acad Sci USA. 2006;103(32):11892-7. doi: 10.1073/pnas.0601708103. PubMed PMID: 16882730; PubMed
944 Central PMCID: PMCPMC2131687.
945 37. Joseph JS, Saikatendu KS, Subramanian V, Neuman BW, Buchmeier MJ, Stevens RC, et al. Crystal
946 structure of a monomeric form of severe acute respiratory syndrome coronavirus endonuclease nsp15 suggests a
947 role for hexamerization as an allosteric switch. J Virol. 2007;81(12):6700-8. Epub 2007/04/06. doi:
948 10.1128/JVI.02817-06. PubMed PMID: 17409150; PubMed Central PMCID: PMCPMC1900129.
949 38. Van Loy B, Stevaert A, Naesens L. The coronavirus nsp15 endoribonuclease: A puzzling protein and
950 pertinent antiviral drug target. Antiviral Res. 2024;228:105921. Epub 20240531. doi:
951 10.1016/j.antiviral.2024.105921. PubMed PMID: 38825019.
952 39. Stevaert A, Krasniqi B, Van Loy B, Nguyen T, Thomas J, Vandeput J, et al. Betulonic acid derivatives
953 interfering with human coronavirus 229E replication via the nsp15 endoribonuclease. J Med Chem.
954 2021;64(9):5632-44. Epub 2021/04/21. doi: 10.1021/acs.jmedchem.0c02124. PubMed PMID: 33877845; PubMed
955 Central PMCID: PMCPMC8084268.
956 40. Vrijens P, Noppen S, Boogaerts T, Vanstreels E, Ronca R, Chiodelli P, et al. Influenza virus entry via the
957 GM3 ganglioside-mediated platelet-derived growth factor receptor beta signalling pathway. J Gen Virol.
958 2019;100(4):583-601. Epub 2019/02/15. doi: 10.1099/jgv.0.001235. PubMed PMID: 30762518.
959 41. Szűcs Z, Naesens L, Stevaert A, Ostorházi E, Batta G, Herczegh P, et al. Reprogramming of the
960 antibacterial drug vancomycin results in potent antiviral agents devoid of antibacterial activity. Pharmaceuticals

961 (Basel). 2020;13(7):139. Epub 2020/07/03. doi: 10.3390/ph13070139. PubMed PMID: 32610683; PubMed Central
962 PMCID: PMCPMC7407158.
963 42. Delang L, Segura Guerrero N, Tas A, Querat G, Pastorino B, Froeyen M, et al. Mutations in the
964 chikungunya virus non-structural proteins cause resistance to favipiravir (T-705), a broad-spectrum antiviral. J
965 Antimicrob Chemother. 2014;69(10):2770-84. doi: 10.1093/jac/dku209. PubMed PMID: 24951535.
966 43. Xie X, Lokugamage KG, Zhang X, Vu MN, Muruato AE, Menachery VD, et al. Engineering SARS-CoV-2
967 using a reverse genetic system. Nat Protoc. 2021;16(3):1761-84. Epub 2021/01/31. doi: 10.1038/s41596-021-
968 00491-8. PubMed PMID: 33514944; PubMed Central PMCID: PMCPMC8168523.
969 44. Li H. New strategies to improve minimap2 alignment accuracy. Bioinformatics. 2021;37(23):4572-4. doi:
970 10.1093/bioinformatics/btab705. PubMed PMID: 34623391; PubMed Central PMCID: PMCPMC8652018.
971 45. Khanna A, Larson D, Srivatsan S, Mosior M, Abbott T, Kiwala S, et al. Bam-readcount - rapid generation
972 of basepair-resolution sequence metrics. J Open Source Softw. 2022;7(69). doi: 10.21105/joss.03722.
973 46. Xu X, Zhai Y, Sun F, Lou Z, Su D, Xu Y, et al. New antiviral target revealed by the hexameric structure of
974 mouse hepatitis virus nonstructural protein nsp15. J Virol. 2006;80(16):7909-17. Epub 2006/07/29. doi:
975 10.1128/JVI.00525-06. PubMed PMID: 16873248; PubMed Central PMCID: PMCPMC1563835.
976 47. Guarino LA, Bhardwaj K, Dong W, Sun J, Holzenburg A, Kao C. Mutational analysis of the SARS virus
977 nsp15 endoribonuclease: identification of residues affecting hexamer formation. J Mol Biol. 2005;353(5):1106-17.
978 Epub 2005/10/12. doi: 10.1016/j.jmb.2005.09.007. PubMed PMID: 16216269.
979 48. Zheng S, Wang W, Aldahdooh J, Malyutina A, Shadbahr T, Tanoli Z, et al. SynergyFinder Plus: Toward
980 better interpretation and annotation of drug combination screening datasets. Genomics Proteomics Bioinformatics.
981 2022;20(3):587-96. Epub 20220125. doi: 10.1016/j.gpb.2022.01.004. PubMed PMID: 35085776; PubMed Central
982 PMCID: PMCPMC9801064.
983 49. Wu Y, Zhang H, Shi Z, Chen J, Li M, Shi H, et al. Porcine epidemic diarrhea virus nsp15 antagonizes
984 interferon signaling by RNA degradation of TBK1 and IRF3. Viruses. 2020;12(6):599. Epub 20200531. doi:
985 10.3390/v12060599. PubMed PMID: 32486349; PubMed Central PMCID: PMCPMC7354440.
986 50. Tao S, Zandi K, Bassit L, Ong YT, Verma K, Liu P, et al. Comparison of anti-SARS-CoV-2 activity and
987 intracellular metabolism of remdesivir and its parent nucleoside. Curr Res Pharmacol Drug Discov. 2021;2:100045.
988 Epub 20210812. doi: 10.1016/j.crphar.2021.100045. PubMed PMID: 34870151; PubMed Central PMCID:
989 PMCPMC8357487.
990 51. van Huizen M, Vendrell XM, de Gruyter HLM, Boomaars-van der Zanden AL, van der Meer Y, Snijder EJ,
991 et al. The main protease of Middle East respiratory syndrome coronavirus induces cleavage of mitochondrial
992 antiviral signaling protein to antagonize the innate immune response. Viruses. 2024;16(2):256. Epub 20240205.
993 doi: 10.3390/v16020256. PubMed PMID: 38400032; PubMed Central PMCID: PMCPMC10892576.

994 52. Liu Y, Qin C, Rao Y, Ngo C, Feng JJ, Zhao J, et al. SARS-CoV-2 Nsp5 demonstrates two distinct
995 mechanisms targeting RIG-I and MAVS to evade the innate immune response. mBio. 2021;12(5):e0233521. Epub
996 20210921. doi: 10.1128/mBio.02335-21. PubMed PMID: 34544279; PubMed Central PMCID: PMCPMC8546575.
997 53. Melano I, Lo YC, Su WC. Characterization of host substrates of SARS-CoV-2 main protease. Front
998 Microbiol. 2023;14:1251705. Epub 20230821. doi: 10.3389/fmicb.2023.1251705. PubMed PMID: 37670988;
999 PubMed Central PMCID: PMCPMC10475589.
1000 54. Song L, Wang D, Abbas G, Li M, Cui M, Wang J, et al. The main protease of SARS-CoV-2 cleaves histone
1001 deacetylases and DCP1A, attenuating the immune defense of the interferon-stimulated genes. J Biol Chem.
1002 2023;299(3):102990. Epub 20230208. doi: 10.1016/j.jbc.2023.102990. PubMed PMID: 36758802; PubMed Central
1003 PMCID: PMCPMC9907797.
1004 55. Shirato K, Kanou K, Kawase M, Matsuyama S. Clinical isolates of human coronavirus 229E bypass the
1005 endosome for cell entry. J Virol. 2017;91(1):e01387-16. Epub 2016/11/01. doi: 10.1128/JVI.01387-16. PubMed
1006 PMID: 27733646; PubMed Central PMCID: PMCPMC5165181.
1007 56. Lundin A, Dijkman R, Bergstrom T, Kann N, Adamiak B, Hannoun C, et al. Targeting membrane-bound
1008 viral RNA synthesis reveals potent inhibition of diverse coronaviruses including the Middle East respiratory
1009 syndrome virus. PLoS Pathog. 2014;10(5):e1004166. doi: 10.1371/journal.ppat.1004166. PubMed PMID:
1010 24874215; PubMed Central PMCID: PMCPMC4038610.
1011 57. Zorn JA, Wells JA. Turning enzymes ON with small molecules. Nat Chem Biol. 2010;6(3):179-88. doi:
1012 10.1038/nchembio.318. PubMed PMID: 20154666.
1013 58. Huang T, Snell KC, Kalia N, Gardezi S, Guo L, Harris ME. Kinetic analysis of RNA cleavage by coronavirus
1014 nsp15 endonuclease: evidence for acid-base catalysis and substrate-dependent metal ion activation. J Biol Chem.
1015 2023;299(6):104787. Epub 20230504. doi: 10.1016/j.jbc.2023.104787. PubMed PMID: 37149147; PubMed Central
1016 PMCID: PMCPMC10158045.
1017 59. Bhardwaj K, Guarino L, Kao CC. The severe acute respiratory syndrome coronavirus Nsp15 protein is an
1018 endoribonuclease that prefers manganese as a cofactor. J Virol. 2004;78(22):12218-24. Epub 2004/10/28. doi:
1019 10.1128/JVI.78.22.12218-12224.2004. PubMed PMID: 15507608; PubMed Central PMCID: PMCPMC525082.
1020 60. Perry JK, Appleby TC, Bilello JP, Feng JY, Schmitz U, Campbell EA. An atomistic model of the coronavirus
1021 replication-transcription complex as a hexamer assembled around nsp15. J Biol Chem. 2021;297(4):101218. Epub
1022 20210923. doi: 10.1016/j.jbc.2021.101218. PubMed PMID: 34562452; PubMed Central PMCID:
1023 PMCPMC8494237.
1024 61. Kang H, Bhardwaj K, Li Y, Palaninathan S, Sacchettini J, Guarino L, et al. Biochemical and genetic
1025 analyses of murine hepatitis virus nsp15 endoribonuclease. J Virol. 2007;81(24):13587-97. Epub 2007/09/28. doi:
1026 10.1128/JVI.00547-07. PubMed PMID: 17898055; PubMed Central PMCID: PMCPMC2168834.

1027 62. Pettersen EF, Goddard TD, Huang CC, Couch GS, Greenblatt DM, Meng EC, et al. UCSF Chimera - a
1028 visualization system for exploratory research and analysis. J Comput Chem. 2004;25(13):1605-12. doi:
1029 10.1002/jcc.20084. PubMed PMID: 15264254.
1030 63. Robert X, Gouet P. Deciphering key features in protein structures with the new ENDscript server. Nucleic
1031 Acids Res. 2014;42(Web Server issue):W320-W4. Epub 2014/04/23. doi: 10.1093/nar/gku316. PubMed PMID:
1032 24753421; PubMed Central PMCID: PMCPMC4086106.

1033

Supporting information

S1 Appendix. Chemical synthesis and analysis of EPB-113 and its two structural analogues EPB-102 and JMLv-061.

S1 Appendix: Chemistry

Table of contents

General methods	S1
Chemical synthesis of **EPB-102**	S2
Chemical synthesis of **EPB-113**	S3
Chemical synthesis of **JMLv-061**	S6
^{1}H, ^{13}C and ^{19}F NMR spectra of **EPB-102**	S8
^{1}H, ^{13}C and ^{19}F NMR spectra of **EPB-113**	S10
^{1}H and ^{13}C spectra of **JMLV-061**	S12
References	S13

Chemical synthesis. General methods.

Commercially available reagents and solvents were used without further purification unless stated otherwise. Preparative normal phase chromatography was performed on a CombiFlash Rf 150 (Teledyne Isco) with pre-packed RediSep Rf silica gel cartridges. Thin-layer chromatography was performed with aluminum-backed sheets with silica gel 60 F_{254} (Merck, ref 1.05554), and spots were visualized with UV light and 1% aqueous solution of $KMnO_4$. Melting points were determined in open capillary tubes with a MFB 595010M Gallenkamp. 400 MHz ^{1}H, 100.6 MHz ^{13}C and 376.5 MHz ^{19}F NMR spectra were recorded on a Varian Mercury 400 or on a Bruker 400 Avance III spectrometers. The chemical shifts are reported in ppm (δ scale) relative to internal tetramethylsilane, and coupling constants are reported in Hertz (Hz). Assignments given for the NMR spectra of the new compounds have been carried out on the basis of COSY $^{1}H/^{13}C$ (gHSQC sequence) experiments. IR spectra were run on a Perkin-Elmer Spectrum RX I spectrophotometer. Absorption values are expressed as wave-numbers (cm^{-1}); only significant absorption bands are given. High-resolution mass spectrometry (HRMS) analyses were performed with an LC/MSD TOF Agilent Technologies spectrometer. The elemental analyses were carried out in a Flash 1112 series Thermofinnigan elemental microanalyzator (A5) to determine C, H, N and S. The structure of all new compounds was confirmed by elemental analysis and/or accurate mass measurement, IR, ^{1}H NMR, ^{13}C NMR and ^{19}F NMR. The analytical samples of all the new compounds, which were subjected to antiviral evaluation, possessed purity ≥ 95% as evidenced by their elemental analyses and/or their HPLC/MS. HPLC/MS for EPB-113 was determined with a HPLC Agilent 1260 Infinity II LC/MSD coupled to a photodiode array and mass spectrometer. 5 µL of sample 0.5 mg/mL in methanol:acetonitrile were injected, using a Agilent Poroshell 120 EC-C18, 2.7 µm, 50 mm x 4.6 mm column at 40 °C. The mobile phase was a mixture of A = water with 0.05% formic acid and B = acetonitrile with 0.05% formic acid, with the method described as follows: flow 0.6 mL/min, from 95% A - 5% B to 100% B in 3 min, 100% B 3 min, from 100% B to 95% A - 5% B in 1 min, 95% A – 5% B 3 min. Purity is given as % of absorbance at 254 nm. Data from mass spectra were analyzed by electrospray ionization in positive and negative between 100 and 1000 Da.

Synthesis of 1-(3-aminophenyl)-3-(3-(pentafluoro-λ^6-sulfanyl)phenyl)urea, EPB-102

Step 1: Synthesis of 1-(3-nitrophenyl)-3-(3-(pentafluoro-λ^6-sulfanyl)phenyl)urea

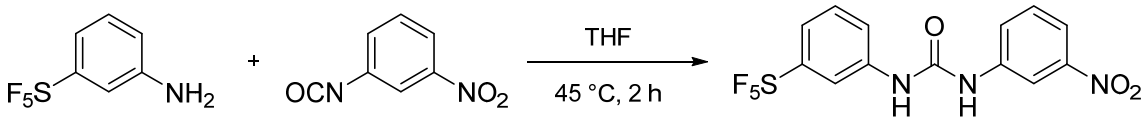

3-Nitrophenylisocyanate (500 mg, 3.05 mmol) was dissolved in THF (25 mL) and 3-pentafluorosulfanyl aniline (668 mg, 3.05 mmol) was added. The reaction mixture was stirred at 45 °C for 2 hours. The solvent was removed under reduced pressure to afford a yellow solid (1.10 g) that was crystallized in EtOAc to give pure 1-(3-nitrophenyl)-3-(3-(pentafluoro-λ^6-sulfanyl)phenyl)urea (1.10 g, 94% yield) as a yellow crystalline solid.

Step 2: Synthesis of EPB-102

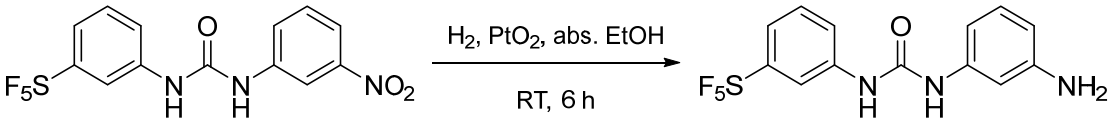

A suspension of 1-(3-nitrophenyl)-3-(3-(pentafluoro-λ^6-sulfanyl)phenyl)urea (600 mg, 1.56 mmol) and PtO_2 hydrate (53 mg) in abs. ethanol (45 mL) was hydrogenated (1 atm) at room temperature for 6 hours. The suspension was then filtered, and the solvent was evaporated under vacuum to afford **EPB-102** (533 mg, 97% yield) as a white solid. The analytical sample was obtained by crystallization from EtOAc, mp (EtOAc) 193–194 °C. IR (ATR) ν: 643, 651, 682, 697, 789, 824, 845, 877, 913, 1167, 1229, 1313, 1420, 1465, 1485, 1566, 1590, 1651, 3092, 3294, 3389, 3489 cm^{-1}. ^{1}H-NMR (400 MHz, DMSO-d_6) δ: 5.05 (s, 2 H, NH_2), 6.21 (m, 1 H, 6-H or 4-H), 6.52 (m, 1 H, 4-H or 6-H), 6.84 (t, J = 2.0 Hz, 1 H, 2-H), 6.90 (t, J = 8.0 Hz, 1 H, 5-H), 7.40-7.55 (complex signal, 3 H, 4'-H, 5'-H, 6'-H), 8.28 (t, J = 2.0 Hz, 1 H, 2'-H), 8.51 (s, 1 H) and 9.03 (s, 1 H) (2 NH). ^{13}C-NMR (100.6 MHz, DMSO-d_6) δ: 104.1 (CH, C2), 106.3 (CH, C4 or C6), 108.4 (CH, C6 or C4), 114.6 (quint, $^3J_{CF}$ = 5.0 Hz, CH, C2'), 118.5 (quint, $^3J_{CF}$ = 3.5 Hz, CH, C4'), 121.5 (CH, C6'), 129.0 (CH, C5), 129.6 (CH, C5'), 139.8 (C, C1), 140.7 (C, C1'), 149.2 (C, C3), 152.3 (C, CO), 153.3 (quint, $^2J_{CF}$ = 15.1 Hz, C, C3'). ^{19}F-NMR (376.5 MHz, DMSO-d_6) δ: 63.6 (d, J = 150.6 Hz, 4 F, S$\underline{F}_4$F), 87.8 (quint, J = 150.6 Hz, 1 F, $SF_4\underline{F}$). HRMS-ESI$^-$ m/z [M-H]$^-$ calculated for [$C_{13}H_{12}F_5N_3OS$-H]$^-$: 352.0548. Found: 352.0554. Elemental analysis calculated for $C_{13}H_{12}F_5N_3OS$: C 44.19%, H 3.42%, N 11.89%, S 9.07%. Found: C 44.24%, H 3.44%, N 11.63%, S 8.78%.

Synthesis of 1-(3-guanidinophenyl)-3-(3-(pentafluoro-λ^6-sulfanyl)-phenyl)urea hydrochloride, EPB-113

Step 1: Synthesis of 2-(3-nitrophenyl)-1,3-di-Boc-guanidine

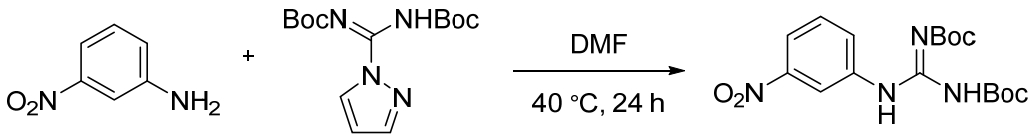

To a stirred solution of 3-nitroaniline (1 g, 7.24 mmol) in DMF (10 mL) was added bis-Boc-pyrazolocarboxamidine (2.25 g, 7.25 mmol) and the reaction mixture was stirred at 40 °C for 24 hours. Water (15 mL) and EtOAc (15 mL) were added, and the phases were separated. The organic layer was further washed with water, dried over anhydrous Na_2SO_4 and filtered. Evaporation of the organics provided a yellowish gum (2.46 g), which was purified by column chromatography in silica gel (hexane/EtOAc mixtures). Fractions containing the desired product were collected and concentrated under vacuum to afford 2-(3-nitrophenyl)-1,3-di-Boc-guanidine (1.0 g, 36% yield) as a yellowish solid. The spectroscopic data matched with those previously described in the bibliography.[1] HRMS-ESI$^+$ *m/z* $[M+H]^+$ calculated for $[C_{17}H_{24}N_4O_6+H]^+$: 381.1769. Found: 381.1769.

Step 2: Obtention of 2-(3-aminophenyl)-1,3-di-Boc-guanidine

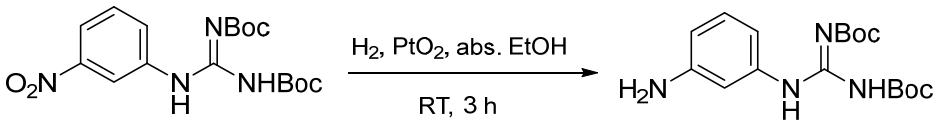

A suspension of 2-(3-nitrophenyl)-1,3-di-Boc-guanidine (1 g, 2.63 mmol) and PtO_2 hydrate (100 mg) in abs. ethanol (100 mL) was hydrogenated (1 atm) at room temperature for 3 hours. The suspension was then filtered, and the solvent was evaporated under vacuum to afford 2-(3-aminophenyl)-1,3-di-Boc-guanidine (0.91 g, quantitative yield) as a white foamy solid. The spectroscopic data matched with those previously described in the bibliography.[2]

Step 3: Synthesis of 1-(1,3-di-Boc-3-guanidinophenyl)-3-(3-(pentafluoro-λ^6-sulfanyl)phenyl)urea

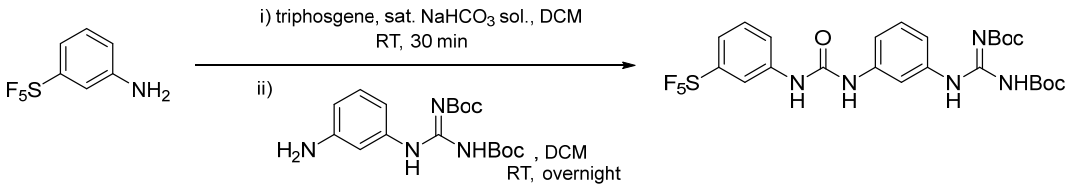

i) 3-pentafluorosulfanyl aniline (80 mg, 0.36 mmol) was added to a stirring biphasic mixture of DCM (5 mL) and saturated aqueous $NaHCO_3$ solution (5 mL). Triphosgene (40 mg, 0.14 mmol) was then slowly added and the reaction mixture was stirred at room temperature for 30 minutes. The phases were separated and the organic layer was washed with brine, dried over anhydrous Na_2SO_4, filtered and half concentrated at room temperature to give 3-(pentafluoro-λ^6-sulfanyl)phenylisocyanate in DCM solution that was used in the next step without further purification.

ii) 2-(3-aminophenyl)-1,3-di-Boc-guanidine (139 mg, 0.40 mmol) dissolved in DCM (2 mL) was added to the previously obtained isocyanate in DCM (ca. 6 mL). The reaction mixture was stirred at room temperature overnight. Evaporation under vacuum of the solvent provided an orange solid (350 mg) which was purified by column chromatography in silica gel (hexane/EtOAc mixtures). Fractions containing the desired product were collected and concentrated under vacuum to give 1-(1,3-di-Boc-3-guanidinophenyl)-3-(3-(pentafluoro-λ^6-sulfanyl)phenyl)urea (60 mg, 29% overall yield) as a yellowish solid. The analytical sample was obtained by washing with Et_2O. ^{1}H-NMR (400 MHz, DMSO-d_6) δ: 1.41 (s, 9 H, Boc), 1.51 (s, 9 H, Boc), 7.15-7.35 (complex signal, 3 H, 2-H, 4-H, 6-H), 7.41-7.59 (complex signal, 3 H, 4'-H, 5-H, 6'-H), 7.64 (s, 1 H, 5'-H), 8.27 (m, 1 H, 2'-H), 8.93 (s, 1 H) and 9.17 (s, 1 H) (2 NH urea), 9.98 (s, 1 H) and 11.35 (s, 1 H) (2 NH guanidine).

Step 4: Synthesis of EPB-113 (as its hydrochloride salt)

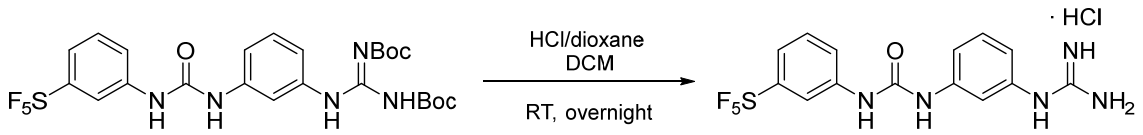

To a stirred suspension of 1-(1,3-di-Boc-3-guanidinophenyl)-3-(3-(pentafluoro-λ^6-sulfanyl)phenyl)urea (32 mg, 0.05 mmol) in DCM (1 mL) was added a 4 M solution of HCl in 1,4-dioxane (4 mL, 16 mmol) and the mixture was stirred at room temperature overnight. Evaporation of the solvents provided a beige solid, which was washed with Et_2O and pentane to give **EPB-113** as its hydrochloride salt (19 mg, 88% yield), mp 219–220 °C. IR (ATR) ν: 754, 782, 812, 835, 857, 916, 1098, 1239, 1296, 1406, 1428, 1484, 1496, 1542, 1587, 1598, 1673, 2966, 3184, 3235, 3416 cm^{-1}. ^{1}H-NMR (400 MHz, DMSO-d_6) δ: 6.86 (m, 1 H, 4-H), 7.27 (m, 1 H, 6-H), 7.35 (t, J = 8.0 Hz, 1 H, 5-H), 7.38 (broad s, 4 H, 2 N$\underline{H}_2$ guanidine), 7.46-7.55 (complex signal, 4 H, 2-H, 4'-H, 5'-H, 6'-H), 8.27 (m, 1 H, 2'-H), 9.31 (s, 1 H) and 9.53 (s, 1 H) (2 NH urea), 9.70 (s, 1 H, 3-NH). ^{13}C-NMR (100.6 MHz, CD_3OD) δ: 117.2 (CH, C2), 117.4 (quint, $^3J_{CF}$ = 5.0 Hz, CH, C2'), 119.4 (CH, C6), 120.5 (CH, C4), 120.9 (quint, $^3J_{CF}$ = 5.0 Hz, CH, C4'), 123.1 (CH, C6'), 130.3 (CH, C5'), 131.4 (CH, C5), 136.6 (C, C1), 141.3 (C, C1'), 142.0 (C, C3), 154.8 (C, CO), 155.4 (quint, $^2J_{CF}$ = 17.1 Hz, C, C3'), 158.0 (C, CN guanidine). ^{19}F-NMR (376.5 MHz, DMSO-d_6) δ: 63.6 (d, J = 150.6 Hz, 4 F, S$\underline{F}_4$F), 87.7 (quint, J = 150.6 Hz, 1 F, SF$_4\underline{F}$). HRMS-ESI$^+$ *m/z* $[M+H]^+$ calculated for $[C_{14}H_{14}F_5N_5OS+H]^+$: 396.0912. Found: 396.0916. HPLC (254 nm): t_R = 3.75 min (98.4%).

Elemental analysis calculated for $C_{14}H_{14}F_5N_5OS \cdot HCl \cdot 0.4H_2O$: C 38.30%, H 3.63%, N 15.95%. Found: C 38.51%, H 3.88%, N 16.21%.

Synthesis of 1-(3-guanidinophenyl)-3-(2-(trifluoromethoxy)phenyl)urea dihydrochloride, JMLV-061

Step 1: Synthesis of 2-(3-nitrophenyl)-1,3-di-Boc-guanidine

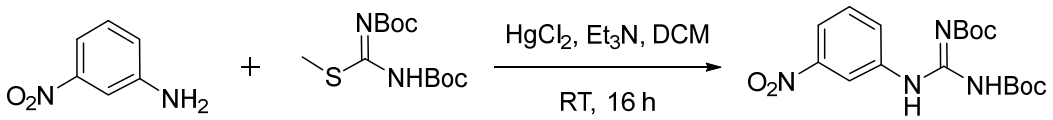

To a solution of 3-nitroaniline (1.50 g, 10.86 mmol) and triethylamine (4.54 mL, 32.58 mmol) in anhydrous DCM (40 mL) was added *N,N'*-bis(tert-butoxycarbonyl)-S-methylisothiourea (3.31 g, 11.40 mmol) and $HgCl_2$ (3.24 g, 11.95 mmol) and the mixture was stirred at RT for 16 hours. The mixture was filtered through a pad of Celite® using DCM as eluting agent. Then, the solution was washed with water (2 x 80 mL). The organic layer was dried over anhydrous Na_2SO_4 and filtered. Solvents were concentrated under vacuum and the resulting crude was purified by column chromatography in silica gel (hexane/EtOAc mixtures). Fractions containing the desired product were collected and concentrated under vacuum to afford 2-(3-nitrophenyl)-1,3-di-Boc-guanidine as a pale-yellow solid (3.88 g, 94% yield). The spectroscopic data matched with those previously described in the bibliography.[1] HRMS-ESI$^+$ *m/z* $[M+H]^+$ calculated for $[C_{17}H_{24}N_4O_6+H]^+$: 381.1769. Found: 381.1769.

Step 2: Obtention of 2-(3-aminophenyl)-1,3-di-Boc-guanidine

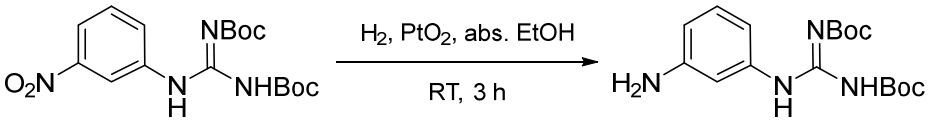

A suspension of 2-(3-nitrophenyl)-1,3-di-Boc-guanidine (2.28 g, 5.99 mmol) and PtO_2 hydrate (250 mg) in abs. ethanol (50 mL) was hydrogenated at room temperature and atmospheric pressure for 3 hours. Anhydrous Na_2SO_4 and Celite® were added and the mixture was stirred for 2 minutes. Then, the suspension was filtered and the solvent was evaporated under vacuum. The resulting crude was purified by column chromatography in silica gel (hexane/EtOAc mixtures). Fractions containing the desired product were collected and concentrated under vacuum to afford 2-(3-aminophenyl)-1,3-di-Boc-guanidine (1.75 g, 83% yield) as a white solid. The spectroscopic data matched with those previously described in the bibliography.[2]

Step 3: Synthesis of JMLV-061 (as its hydrochloride)

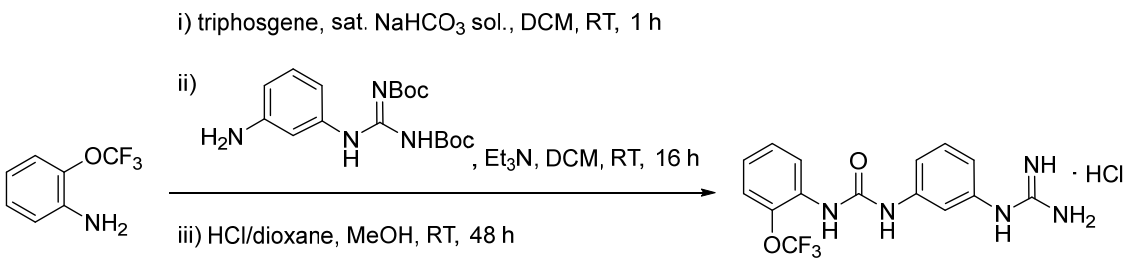

i) To a stirring biphasic mixture of DCM (3 mL), saturated aqueous $NaHCO_3$ solution (3 mL) and triphosgene (101 mg, 0.34 mmol) was added 2-(trifluoromethoxy)aniline (93 µL, 120 mg, 0.68 mmol) portionwise. The mixture was then stirred at room temperature for 1 hour. The phases were separated and the organic layer was washed with brine, dried over anhydrous Na_2SO_4 and filtered. Solvent was concentrated until 1 mL of DCM was left to give 2-(trifluoromethoxy)phenylisocyanate in solution that was used in the next step without further purification.

ii) 2-(3-aminophenyl)-1,3-di-Boc-guanidine (80 mg, 0.23 mmol) and triethylamine (128 µL, 93 mg, 0.92 mmol) dissolved in DCM (2 mL) was added to the previous isocyanate solution and the mixture was stirred at room temperature for 16 hours. Saturated aqueous $NaHCO_3$ solution (15 mL) followed by DCM (10 mL) were added to the mixture and layers were separated. The organic layer was washed again with saturated aqueous $NaHCO_3$ solution (15 mL). Then, the organic layer was separated, dried over anhydrous Na_2SO_4, filtered and solvents were concentrated under vacuum to afford 1-(1,3-di-Boc-3-guanidinophenyl)-3-(2-(trifluoromethoxy)phenyl)urea that was used in the next step without further purification.

iii) A 4 M solution of HCl/1,4-dioxane (2 mL) and MeOH (0.5 mL) were added to the previously obtained crude and the mixture was stirred at room temperature for 48 hours. The solvents were concentrated under vacuum and the resulting crude was purified by column chromatography in silica gel (DCM/MeOH mixtures). Fractions containing the desired product were collected and concentrated under vacuum to afford **JMLv-061** in its dihydrochloride salt as a beige solid (39 mg, 48% yield), mp 218–219 °C. IR (ATR) ν: 624, 691, 758, 871, 1006, 1059, 1180, 1215, 1314, 1406, 1454, 1490, 1540, 1598, 1674, 2421, 3200, 3330 cm^{-1}. ^{1}H-NMR (400 MHz, CD_3OD) δ: 6.95 (ddd, *J* = 8.0 Hz, *J'* = 2.1 Hz, *J''* = 1.0 Hz, 1 H, 4-H), 7.11 (ddd, *J* = 8.1 Hz, *J'* = 7.5 Hz, *J''* = 1.6 Hz, 1 H, 4'-H), 7.29 (m, 1 H, 6-H), 7.30-7.34 (complex signal, 2 H, 3'-H, 5'-H), 7.40 (t, *J* = 8.0 Hz, 1 H, 5-H), 7.64 (t, *J* = 2.1 Hz, 1 H, 2-H), 8.20 (dd, *J* = 8.8 Hz, *J'* = 1.6 Hz, 1 H, 6'-H). ^{13}C-NMR (100.6 MHz, CD_3OD) δ: 116.8 (CH, C2), 119.0 (CH, C6), 120.4 (CH, C4), 122.11 (q, $^1J_{CF}$ = 256.5 Hz, C, OCF_3), 122.13 (CH, C3'), 123.1 (CH, C6'), 124.4 (CH, C4'), 128.7 (CH, C5'), 131.5 (CH, C5), 133.1 (C, C1'), 136.7 (C, C1), 139.9 (C, C2'), 142.1 (C, C3), 154.6 (C, CO), 158.0 (C, CN guanidine). HRMS-ESI$^+$ *m/z* $[M+H]^+$ calculated for $[C_{15}H_{14}F_3N_5O_2+H]^+$: 354.1172. Found: 354.1174. Elemental analysis calculated for $C_{15}H_{14}F_3N_5O_2 \cdot HCl \cdot 0.6DCM$: C 42.51%, H 3.70%, N 15.89%. Found: C 42.38%, H 3.90%, N 15.70%.

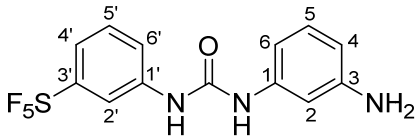
5'
4'
6'
O
6
5
4
3'
1'
1
3
F5S
2'
N
H
N
H
2
NH2

EPB-102

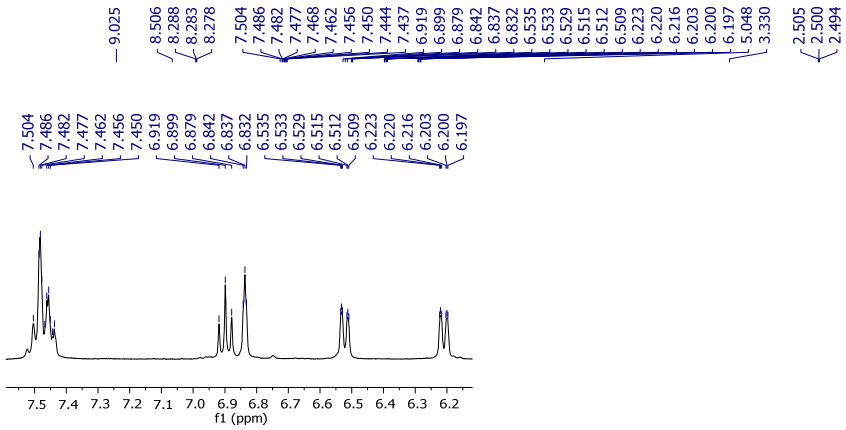
9.025
8.506
8.288
8.283
8.278
7.504
7.486
7.482
7.477
7.468
7.462
7.456
7.450
7.444
7.437
6.919
6.899
6.879
6.842
6.837
6.832
6.535
6.533
6.529
6.515
6.512
6.509
6.223
6.220
6.216
6.203
6.200
6.197
5.048
3.330
2.505
2.500
2.494
7.5 7.4 7.3 7.2 7.1 7.0 6.9 6.8 6.7 6.6 6.5 6.4 6.3 6.2
f1 (ppm)

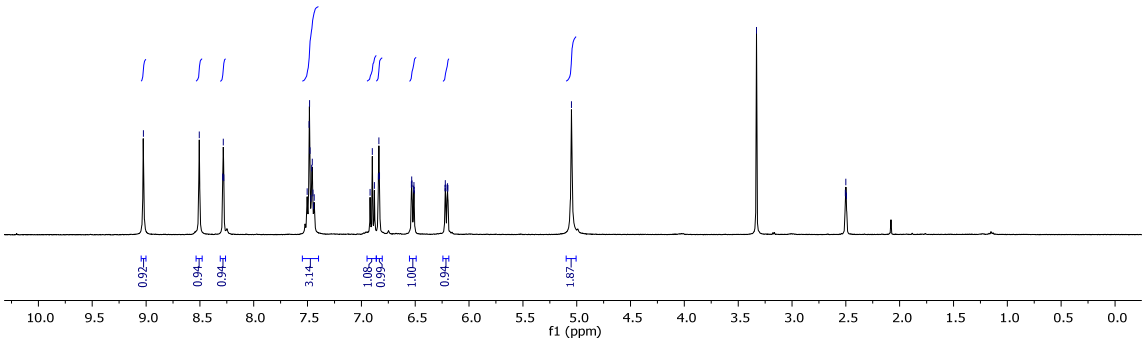
0.92
0.94
0.94
3.14
1.08
0.99
1.00
0.94
1.87
10.0 9.5 9.0 8.5 8.0 7.5 7.0 6.5 6.0 5.5 5.0 4.5 4.0 3.5 3.0 2.5 2.0 1.5 1.0 0.5 0.0
f1 (ppm)

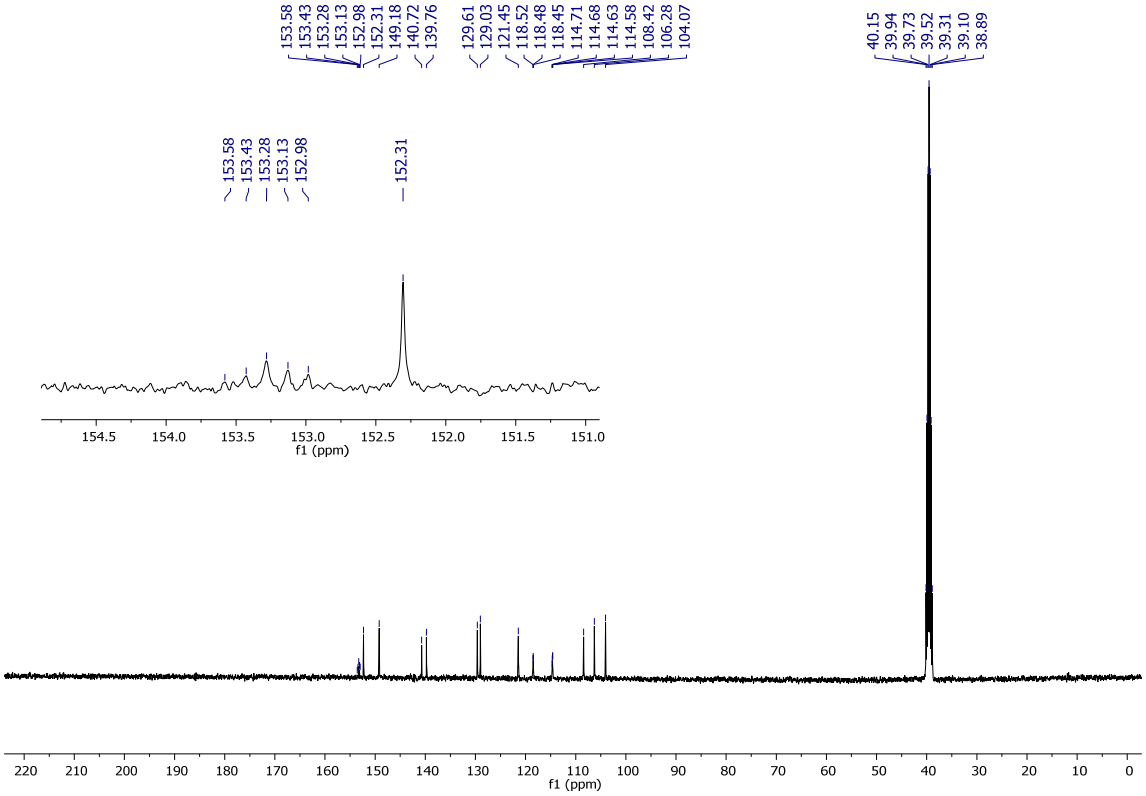
153.58
153.43
153.28
153.13
152.98
152.31
149.18
140.72
139.76
129.61
129.03
121.45
118.52
118.48
118.45
114.71
114.68
114.63
114.58
108.42
106.28
104.07
40.15
39.94
39.73
39.52
39.31
39.10
38.89
154.5 154.0 153.5 153.0 152.5 152.0 151.5 151.0
f1 (ppm)
220 210 200 190 180 170 160 150 140 130 120 110 100 90 80 70 60 50 40 30 20 10 0
f1 (ppm)

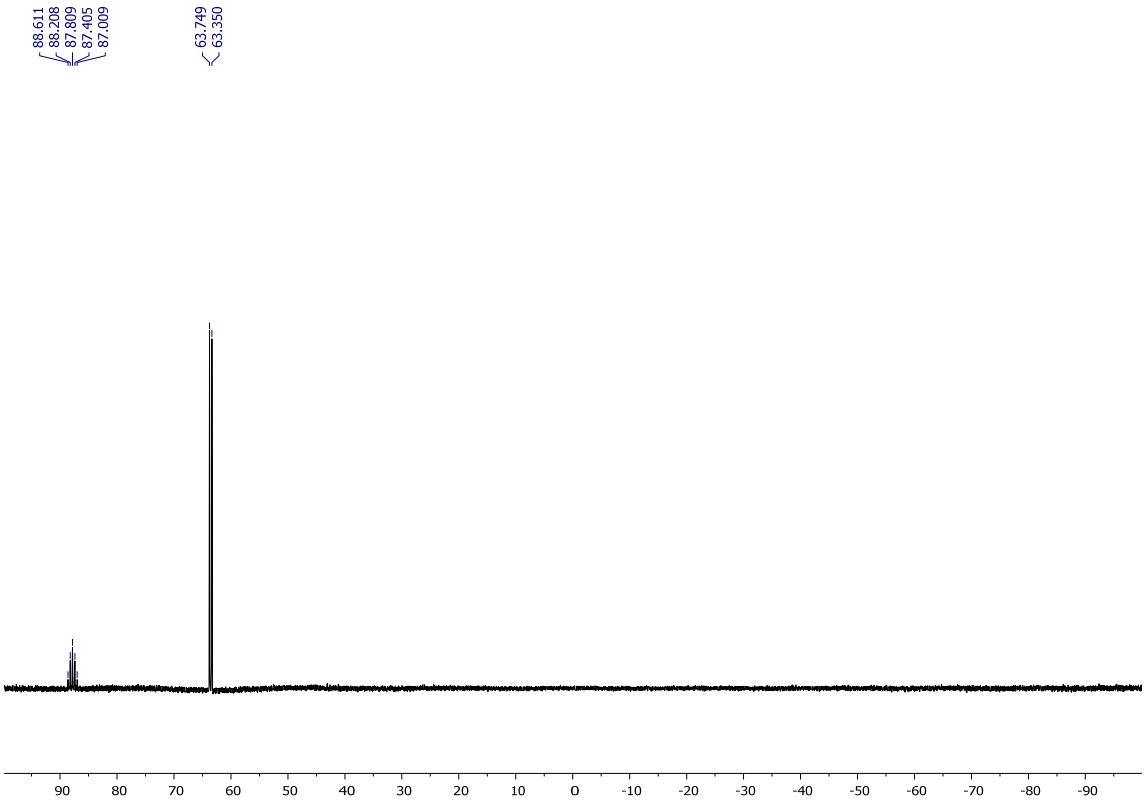
88.611
88.208
87.809
87.405
87.009
63.749
63.350
90 80 70 60 50 40 30 20 10 0 -10 -20 -30 -40 -50 -60 -70 -80 -90

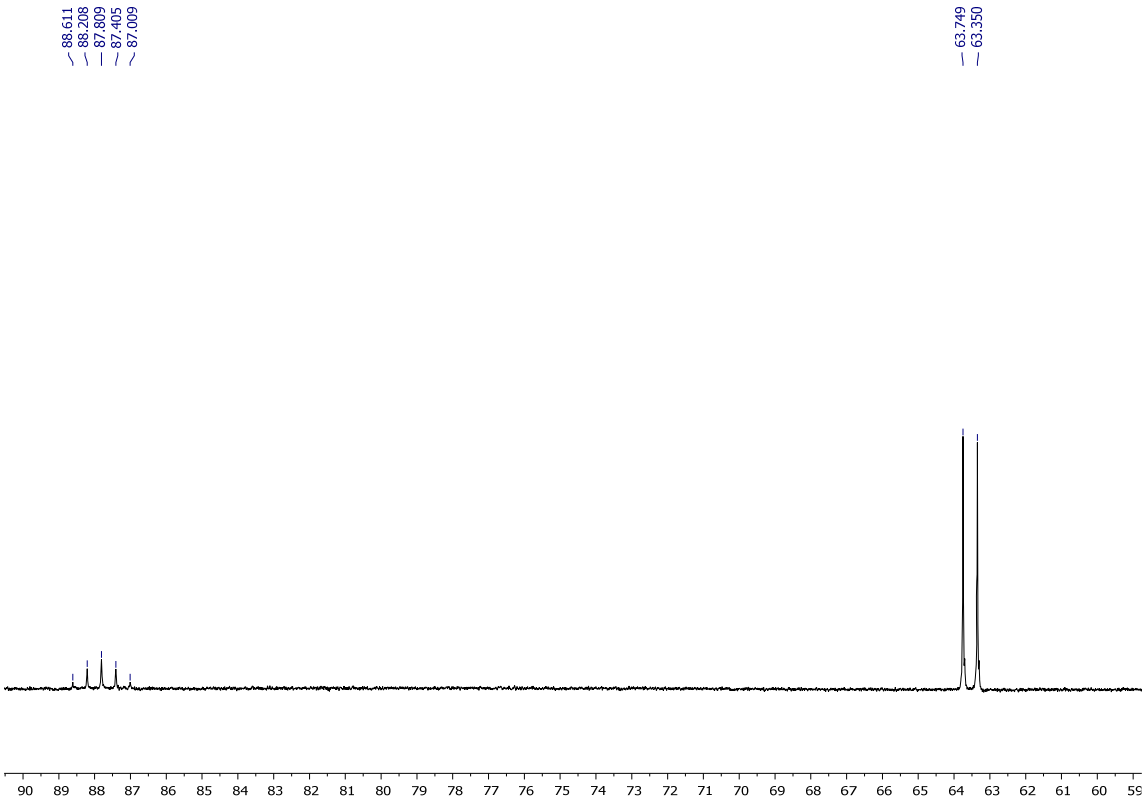
88.611
88.208
87.809
87.405
87.009
63.749
63.350
90 89 88 87 86 85 84 83 82 81 80 79 78 77 76 75 74 73 72 71 70 69 68 67 66 65 64 63 62 61 60 59

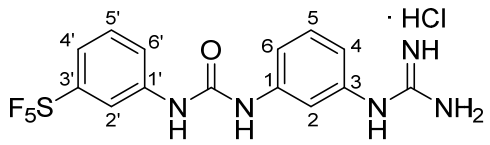
5'
4'
6'
3'
1'
2'
F5S
N
H
O
N
H
5
6
4
1
3
2
N
H
· HCl
NH
NH2

EPB-113

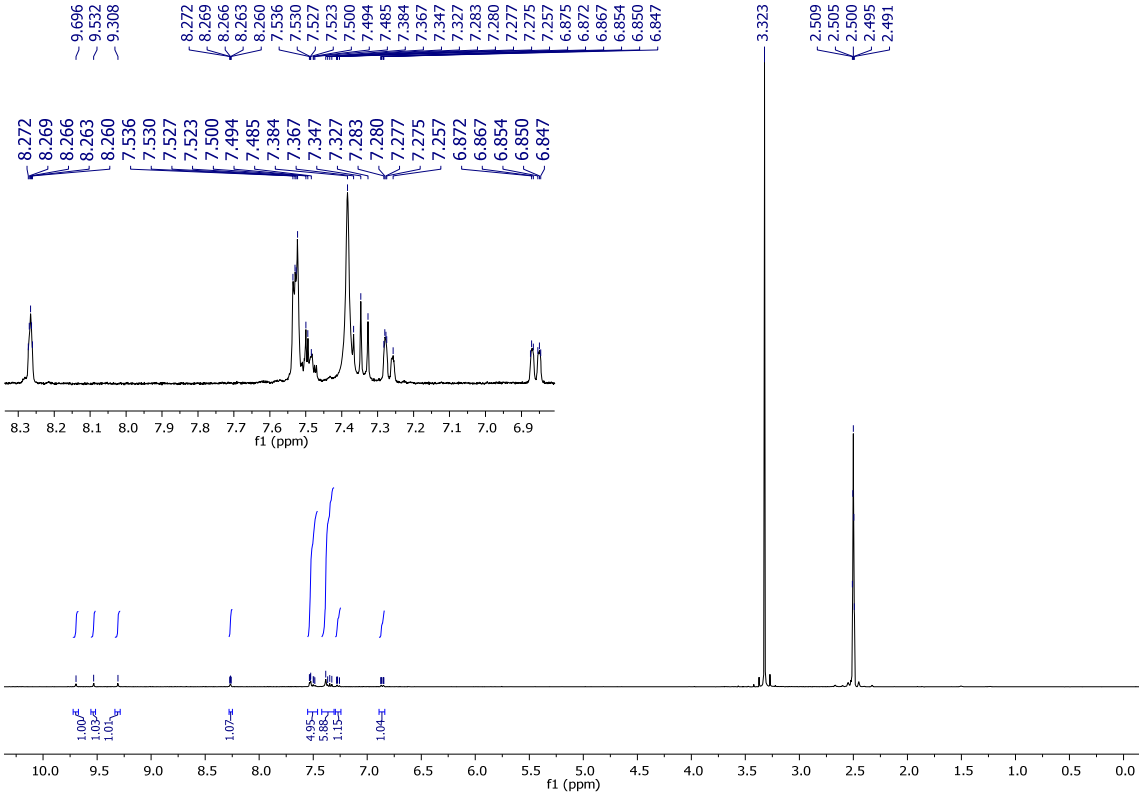
9.696
9.532
9.308
8.272
8.269
8.266
8.263
8.260
7.536
7.530
7.527
7.523
7.500
7.494
7.485
7.384
7.367
7.347
7.327
7.283
7.280
7.277
7.275
7.257
6.875
6.872
6.867
6.854
6.850
6.847
3.323
2.509
2.505
2.500
2.495
2.491
1.00
1.03
1.01
1.07
4.95
5.88
1.15
1.04
f1 (ppm)

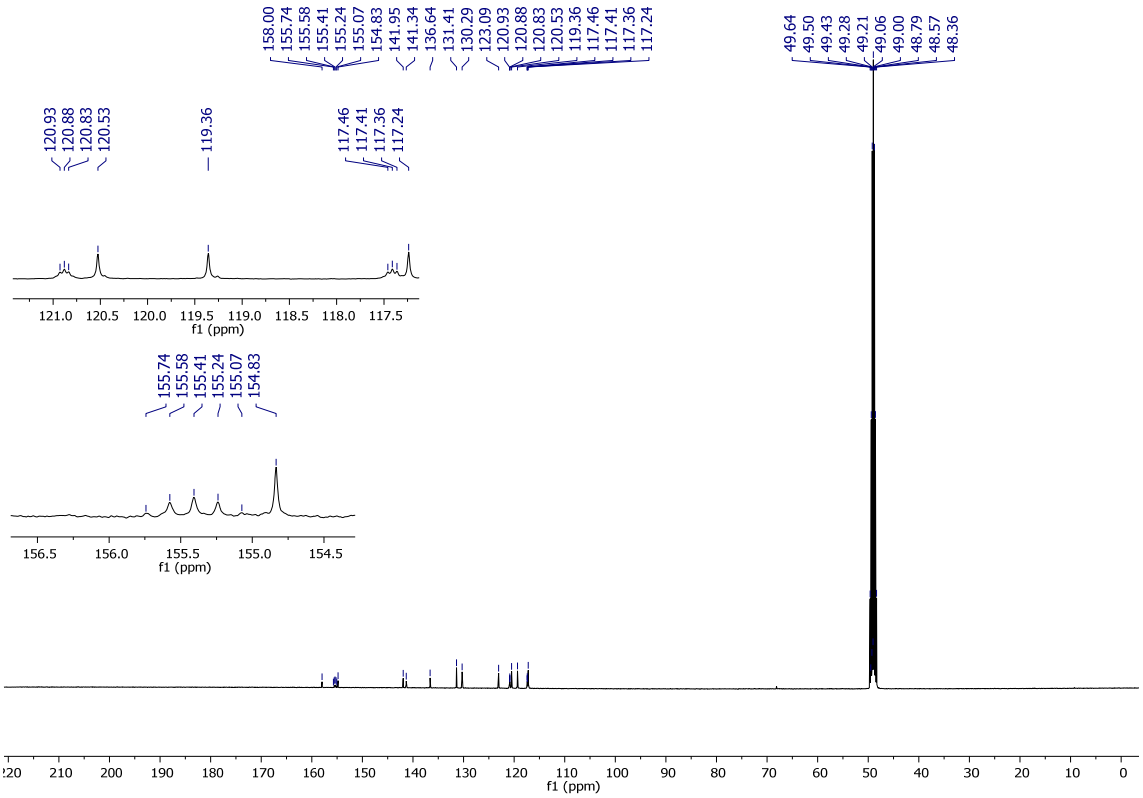
158.00
155.74
155.58
155.41
155.24
155.07
154.83
141.95
141.34
136.64
131.41
130.29
123.09
120.93
120.88
120.83
120.53
119.36
117.46
117.41
117.36
117.24
49.64
49.50
49.43
49.28
49.21
49.06
49.00
48.79
48.57
48.36
f1 (ppm)

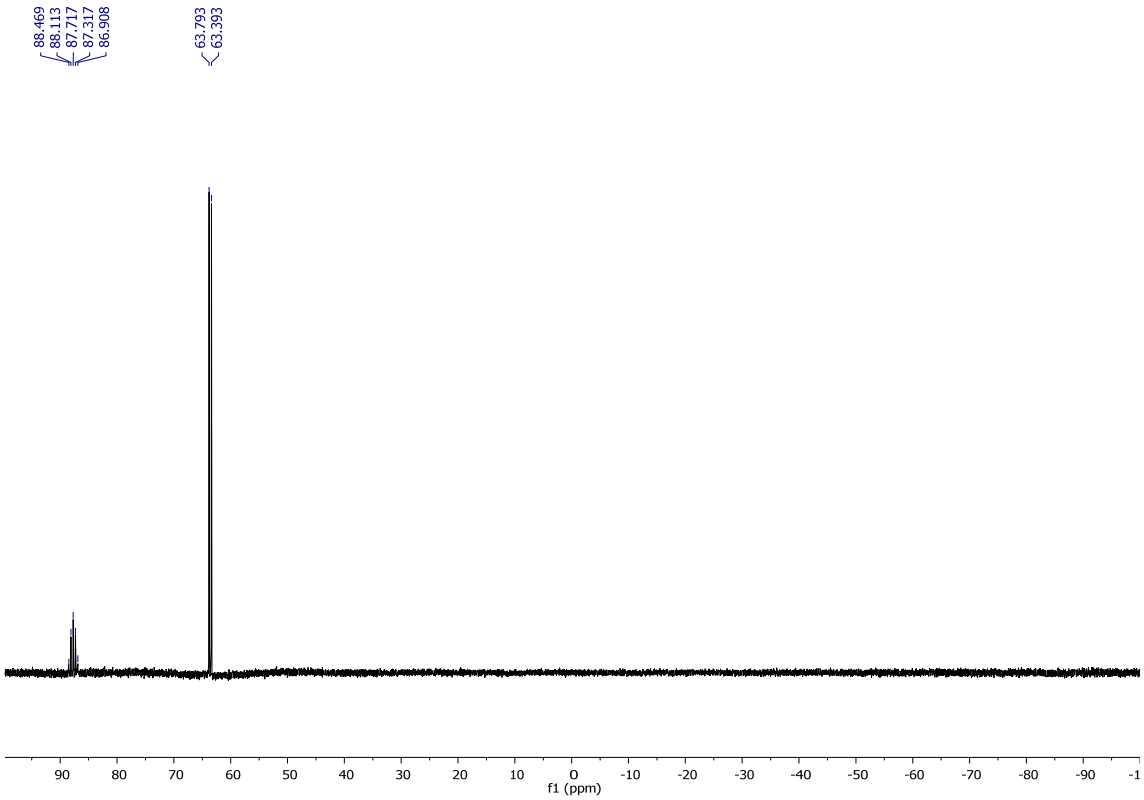
88.469
88.113
87.717
87.317
86.908
63.793
63.393
90 80 70 60 50 40 30 20 10 0 -10 -20 -30 -40 -50 -60 -70 -80 -90 -1
f1 (ppm)

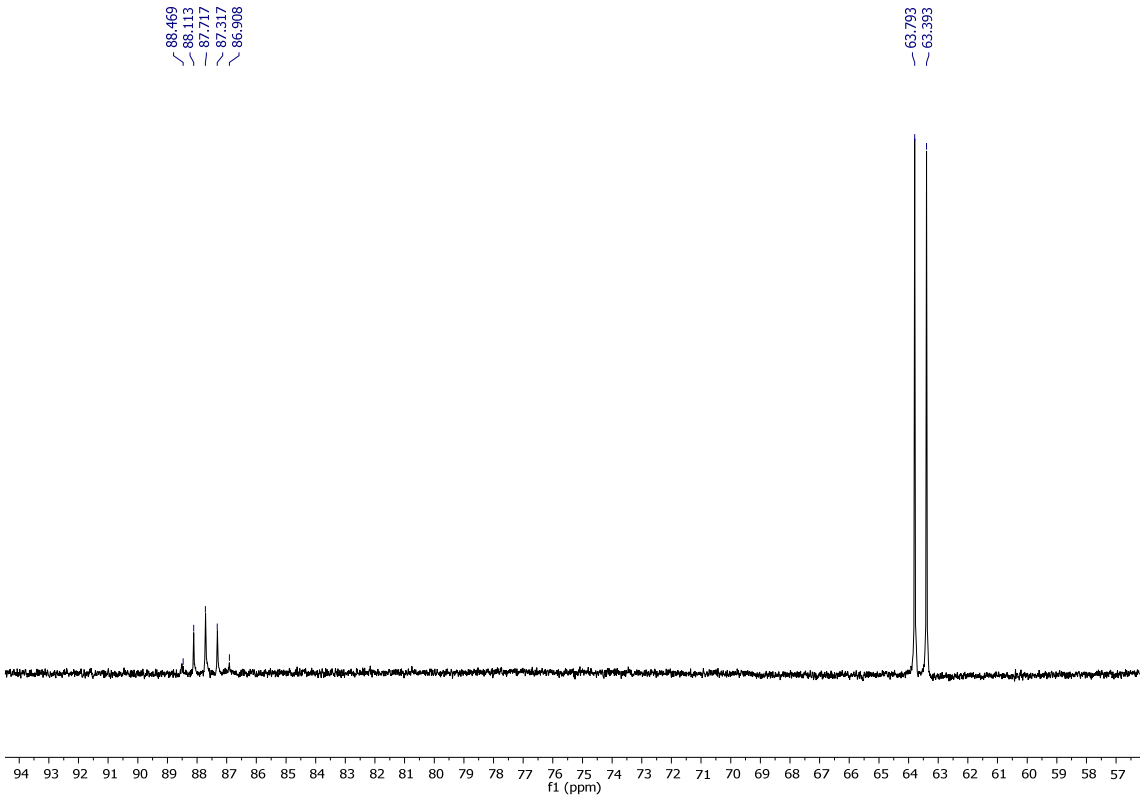
88.469
88.113
87.717
87.317
86.908
63.793
63.393
94 93 92 91 90 89 88 87 86 85 84 83 82 81 80 79 78 77 76 75 74 73 72 71 70 69 68 67 66 65 64 63 62 61 60 59 58 57
f1 (ppm)

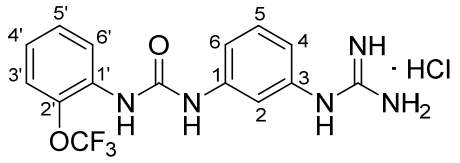
5'
4'
6'
3'
1'
2'
OCF3
O
N
H
N
H
6
5
4
1
3
2
NH
· HCl
N
H
NH2

JMLV-061

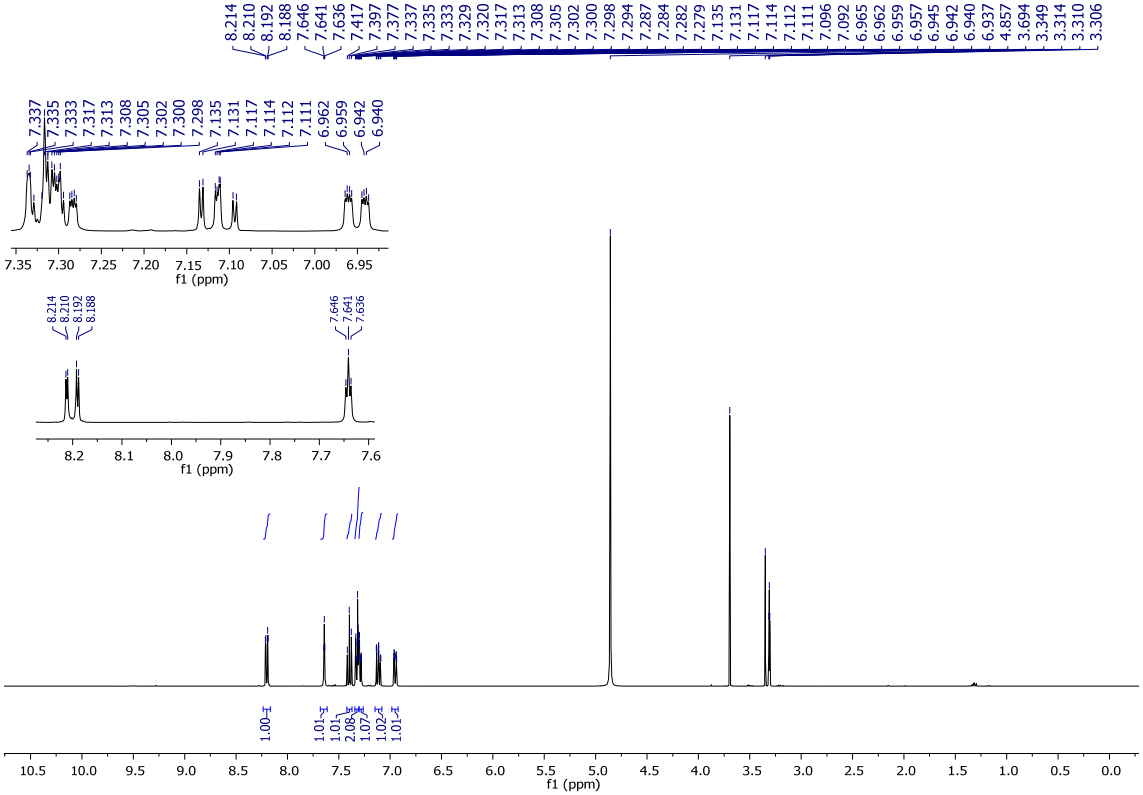
8.214
8.210
8.192
8.188
7.646
7.641
7.636
7.417
7.397
7.377
7.337
7.335
7.333
7.329
7.320
7.317
7.313
7.308
7.305
7.302
7.300
7.298
7.294
7.287
7.284
7.282
7.279
7.135
7.131
7.117
7.114
7.112
7.111
7.096
7.092
6.965
6.962
6.959
6.957
6.945
6.942
6.940
6.937
4.857
3.694
3.349
3.314
3.310
3.306
1.00
1.01
1.01
2.08
1.07
1.02
1.01
f1 (ppm)

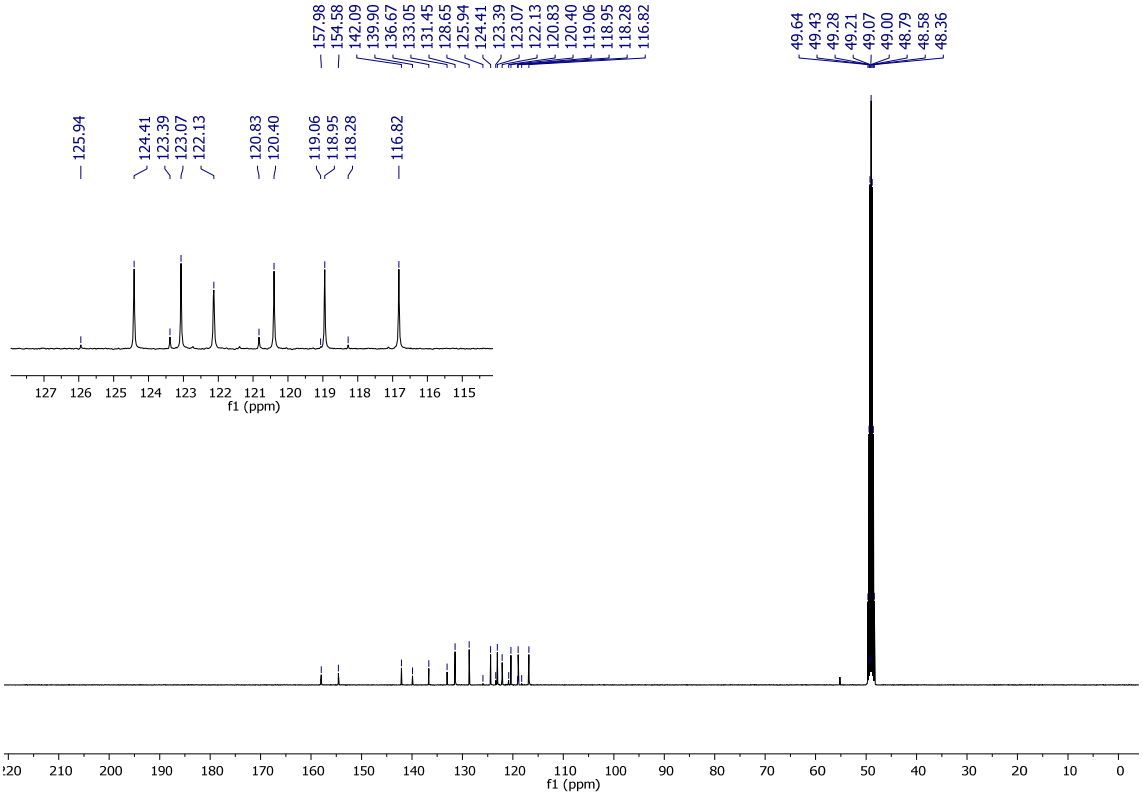
157.98
154.58
142.09
139.90
136.67
133.05
131.45
128.65
125.94
124.41
123.39
123.07
122.13
120.83
120.40
119.06
118.95
118.28
116.82
49.64
49.43
49.28
49.21
49.07
49.00
48.79
48.58
48.36
f1 (ppm)

References

1. Guo Z-X, Cammidge AN, Horwell DC. A convenient and versatile method for the synthesis of protected guanidines. Synt. Commun. 2000;30(16):2933-2943.

2. Kaloun EB, Schmitt P, Kruczynski, A. Isoquinolinone derivatives useful in the treatment of cancer. US9944641B2 (Patent) 2014.

S2 Appendix. Primer and probe sequences. Oligonucleotide sequences used for sequencing or (RT-)qPCR.

S2 Appendix: Primer and probe sequences

One-Step RT-PCR for sequencing of HCoV-229E: five primer pairs

Fragment 1	229E-For84	CTATGGCCGGCATCTTTGA	and	229E-Rev6270	CAAGCAGCCACCACTTAGAT
Fragment 2	229E-For5967	CAGTTGTTATGGTTGGTGGTTATG	and	229E-Rev12295	TATGTGTCCTGCGTAGTGTTG
Fragment 3	229E-For11960	GAACCACCTTGCAGATTTGTTATAG	and	229E-Rev18300	GACCCACCATTTACACCTTCA
Fragment 4	229E-For17743	GTTGCTTCTGGTGATGCTATTATG	and	229E-Rev24484	ACGTACAAGTCGTTAGTTGAGAG
Fragment 5	229E-For23936	TCAGTCGTGCTCATCTTTGTG	and	229E-Rev27281	TTTGTGTATCCATATCGAAACCGT

Sequencing of PCR fragments HCoV-229E

Fragment 1	229E-For84	CTATGGCCGGCATCTTTGA
	229E-Rev454	AACGATGCAATCCTGCAAATC
	229E-For854	CTACGCAATGGTTCTGTTCTTG
	229E-For1679	GACGTGTTTGTCACAGCTATTC
	229E-For2527	CACACAACAGGGTTTGCTTG
	229E-For3251	TCTGAATGGCCTCTTTCTGTTC
	229E-For4100	GAGAAGTTGAACGCCTTCCT
	229E-For4910	TGTGTTGTGCCATCCGAAA
	229E-For5709	ATGGTGTGCAAGTTGGTTATTG
Fragment 2	229E-For5967	CAGTTGTTATGGTTGGTGGTTATG
	229E-For6682	GATGAACTGCTTGTCACTGTTATT
	229E-For6757	CCCAGATTGTATTGCGTGTTC
	229E-For7617	CTGCTGAAGGTCGCAAGTAT
	229E-For8353	GCGTACTATTGCCACCAAATAC
	229E-For9213	CATCTGGCTTTGTGGAGAAATG
	229E-For9947	ACTGGTGTCTGTGTGGAAAG
	229E-For10793	TGTGTTAGTCCAGCCGAATTTA
	229E-For11627	GCTGGTGTTGTTTGGACATTAC
Fragment 3	229E-For11960	GAACCACCTTGCAGATTTGTTATAG
	229E-For12789	GCATGAGGGCAGAACCATTTA
	229E-For13635	GCCTGCCTTGGTGGATAAA
	229E-For14371	CGTATGTTGTCGGCTATGATCT
	229E-For15277	GCTGCTGGTCTTTGTGTAGTA
	229E-For15995	CAATGGCAAACCAGGAGAAATA
	229E-For16796	GGAGCAAGGCTGTGTTTATCT
	229E-For17590	GCTGGCTCATCTGATGTACTG
Fragment 4	229E-For17992	CGCACTGTGCAGAGTCATATT
	229E-For18811	GGTTTAACACCACCTCTCAGTAT
	229E-Rev19020	TCACAGCAGTAGCAGAGAATAAC
	229E-For19607	GGAGATGGATGCTATGGTGTAAAG
	229E-For20359	TGGCGTAACTCCACTGTTATG
	229E-For21258	GTACTGTTGCGTTAGCTTCTTATG
	229E-For22032	AGGGCACCATCTACTCTATCA
	229E-For22846	AGGTCTAACATCAGCCGTTTC
	229E-For23498	CGACAACCTAATCTTGCTCTTTAC
Fragment 5	229E-For23936	TCAGTCGTGCTCATCTTTGTG
	229E-For24698	CACCCAGCTGTTGGAATAGT
	229E-For25507	CGTGCCGAGCACTACTATAA
	229E-For26311	GTACTCCTAAGCCTTCTCGTAATC
	229E-Rev27281	TTTGTGTATCCATATCGAAACCGT

RT-qPCR for HCoV-229E

For	TTAGAGAGCGTGTTGAAGGTG
Rev	GTTCTGAATTCTTGCGCCTAAC
Probe	FAM-TCTGGGTTG/Zen/CTGTTGATGGTGCTA-3IABkFQ

RT-qPCR for SARS-CoV-2[1]

For	TTACAAACATTGGCCGCAAA
Rev	GCGCGACATTCCGAAGAA
Probe	FAM-ACAATTTGC/Zen/CCCCAGCGCTTCAG-3IABkFQ

[1]Lu X, Wang L, Sakthivel SK, Whitaker B, Murray J, Kamili S, et al. US CDC real-time reverse transcription PCR panel for detection of Severe Acute Respiratory Syndrome Coronavirus 2. Emerg Infect Dis. 2020;26(8):1654-65. doi: 10.3201/eid2608.201246.

qPCR for innate immune factors

hACTB_for	CACCATTGGCAATGAGCGGTTC
hACTB_rev	AGGTCTTTGCGGATGTCCACGT
hHPRT_for	CATTATGCTGAGGATTTGGAAAGG
hHPRT_rev	CTTGAGCACACAGAGGGCTACA
hRIGI_for	CACCTCAGTTGCTGATGAAGGC
hRIGI_rev	GTCAGAAGGAAGCACTTGCTACC
hMDA5_for	GCTGAAGTAGGAGTCAAAGCCC
hMDA5_rev	CCACTGTGGTAGCGATAAGCAG
hMAVS_for	ATGGTGCTCACCAAGGTGTCTG
hMAVS_rev	TCTCAGAGCTGCTGTCTAGCCA
hIRF3_for	TCTGCCCTCAACCGCAAAGAAG
hIRF3_rev	TACTGCCTCCACCATTGGTGTC
hIRF7_for	CCACGCTATACCATCTACCTGG
hIRF7_rev	GCTGCTATCCAGGGAAGACACA
hIFNB_for	CTTGGATTCCTACAAAGAAGCAGC
hIFNB_rev	TCCTCCTTCTGGAACTGCTGCA
hOAS1_for	AGGAAAGGTGCTTCCGAGGTAG
hOAS1_rev	GGACTGAGGAAGACAACCAGGT
hOAS2_for	GCTTCCGACAATCAACAGCCAAG
hOAS2_rev	CTTGACGATTTTGTGCCGCTCG
hOAS3_for	CCTGATTCTGCTGGTGAAGCAC
hOAS3_rev	TCCCAGGCAAAGATGGTGAGGA
hRNaseL_for	AAGGCTGTTCAAGAACTACACTTG
hRNaseL_rev	TGGATCTCCAGCCCACTTGATG
hPKR_for	GAAGTGGACCTCTACGCTTTGG
hPKR_rev	TGATGCCATCCCGTAGGTCTGT

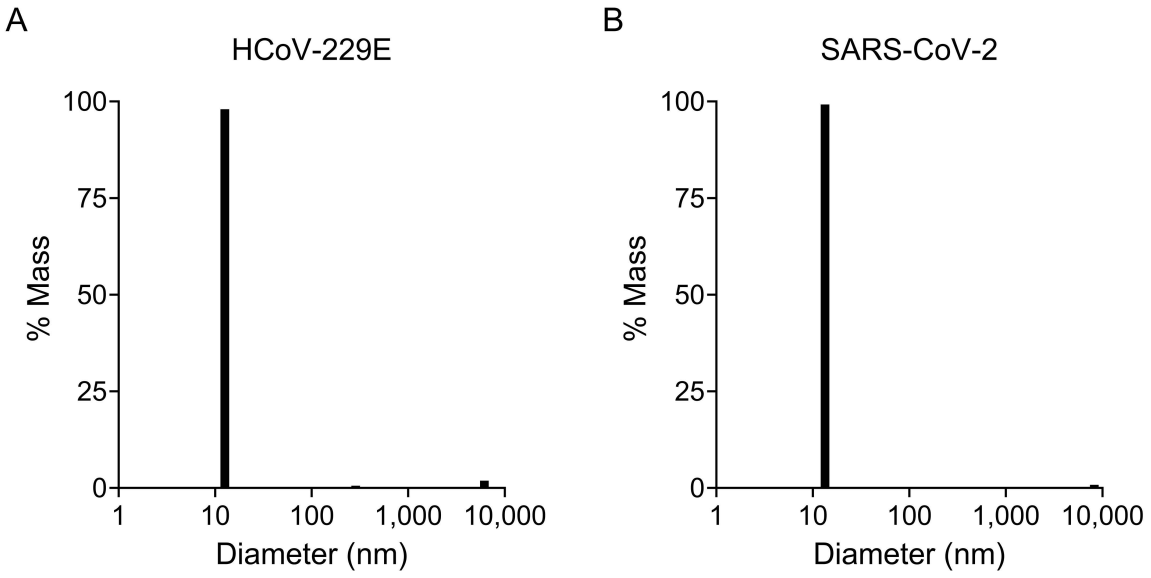

S1 Fig. Particle size distribution of SEC-purified nsp15 samples

Particle size distribution of HCoV-229E and SARS-CoV-2 nsp15 as determined by dynamic light scattering (DLS). Cuvette-based DLS was performed on SEC-purified 0.5 mg/ml nsp15 solutions in storage buffer (25 mM HEPES at pH 8, 300 mM NaCl, 10% glycerol, and 1 mM tris(2-carboxyethyl)phosphine), using a DynaPro Nanostar and Dynamics software v7.10.1.21 (Wyatt Technologies). 15 µl of sample was mixed 5 µl water. The sample chamber was kept at 20 °C. The sample contained ≥ 98% particles with a diameter of ~13 nm, consistent with the size of hexameric nsp15, for both HCoV-229E (polydispersity index: 9%) and SARS-CoV-2 (polydispersity index: 11.7%).

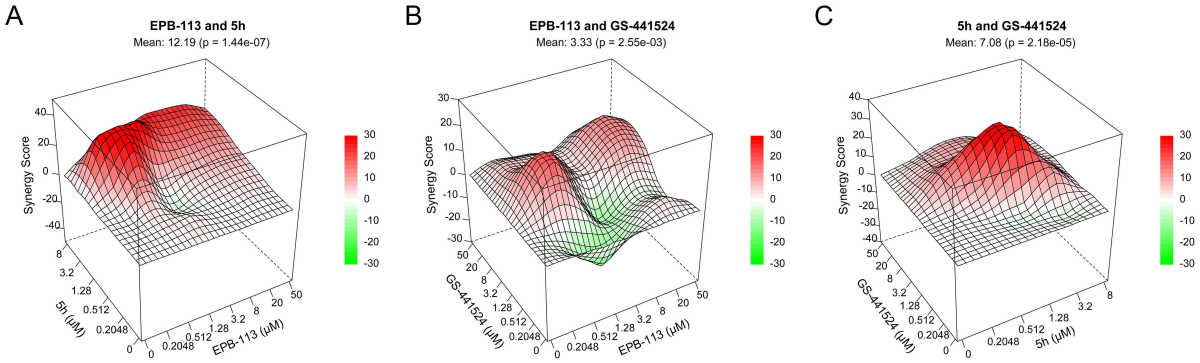

S2 Fig. Synergism analysis of EPB-113, 5h and GS-441524.

To study drug combinations, we used an alternative CPE reduction assay with HCoV-229E in HEL299 cells. An 8x8-well matrix was created, each well containing different concentrations of two compounds. Data analysis was performed with the zero-interaction potency (ZIP) model in SynergyFinder+. Mean ZIP-scores are shown on top of each graph. A ZIP-score lower than -10 indicates antagonism, between -10 and 10 corresponds with additive effects, and higher than 10 indicates synergism. The combination of EPB-113 with 5h is synergistic (A), while the combinations of EPB-113 with GS-441524 (B) and 5h with GS-441524 (C) are additive.

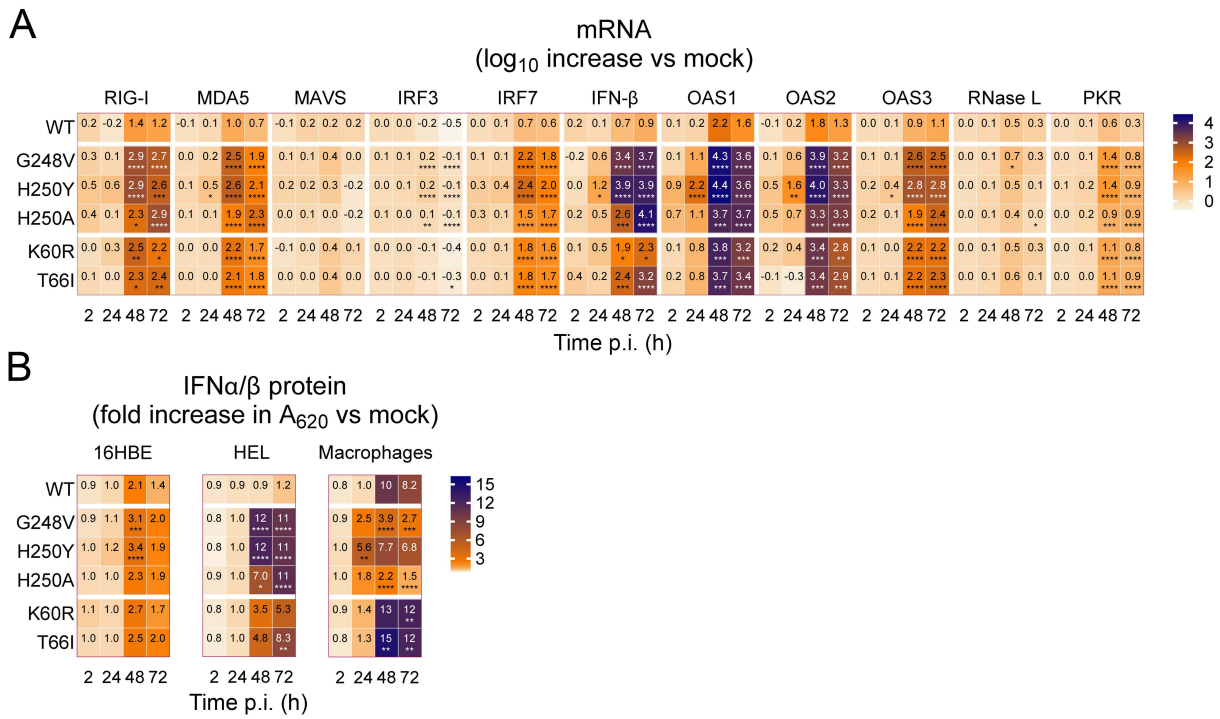

S3 Fig. Numeric values used to create the heatmap in Fig. 4, and statistical analysis of the data.

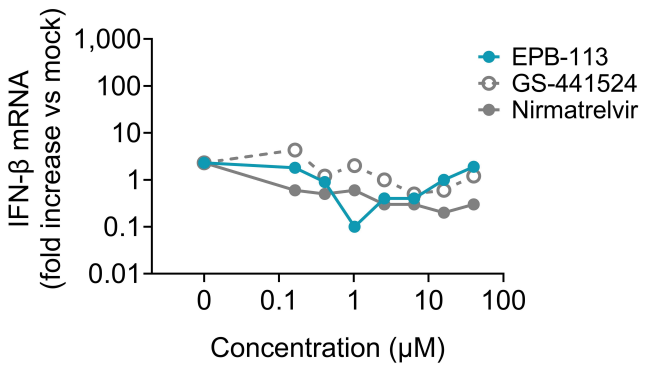

S4 Fig. EPB-113, nirmatrelvir and GS-441524 do not increase IFN-β mRNA levels in HEL299 cells when compound and HCoV-229E virus are added simultaneously.